

Review article

Joshua D. Caldwell*, Lucas Lindsay, Vincenzo Giannini, Igor Vurgaftman, Thomas L. Reinecke, Stefan A. Maier and Orest J. Glembocki

Low-loss, infrared and terahertz nanophotonics using surface phonon polaritons

Abstract: The excitation of surface-phonon-polariton (SPhP) modes in polar dielectric crystals and the associated new developments in the field of SPhPs are reviewed. The emphasis of this work is on providing an understanding of the general phenomenon, including the origin of the Reststrahlen band, the role that optical phonons in polar dielectric lattices play in supporting sub-diffraction-limited modes and how the relatively long optical phonon lifetimes can lead to the low optical losses observed within these materials. Based on this overview, the achievements attained to date and the potential technological advantages of these materials are discussed for localized modes in nanostructures, propagating modes on surfaces and in waveguides and novel metamaterial designs, with the goal of realizing low-loss nanophotonics and metamaterials in the mid-infrared to terahertz spectral ranges.

Keywords: Reststrahlen; phonon polariton; plasmonics; polar dielectric; nanophotonic; metamaterial; infrared; terahertz.

DOI 10.1515/nanoph-2014-0003

Received January 29, 2014; accepted July 19, 2014

***Corresponding author: Joshua D. Caldwell**, U.S. Naval Research Laboratory, 4555 Overlook Ave, S.W. Washington District of Columbia 20375, Washington, D.C. USA, Tel.: +202-404-6209, e-mail: joshua.caldwell@nrl.navy.mil

Lucas Lindsay: NRC Postdoctoral Fellow residing at NRL, Washington, D.C., USA

Vincenzo Giannini and Stefan A. Maier: The Blackett Laboratory, Department of Physics, Imperial College London, London, UK

Igor Vurgaftman, Thomas L. Reinecke and Orest J. Glembocki: U.S. Naval Research Laboratory, 4555 Overlook Ave S.W., Washington, D.C., USA

Edited by Uriel Levy

1 Introduction to surface phonon polaritons

The observation that surface plasmon polaritons (SPPs) could be stimulated on a metal surface [1] with sub-diffraction confinement of the optical fields, as well as the later discoveries of the surface enhanced Raman scattering (SERS) effect [2, 3] and the extraordinary optical transmission response of sub-wavelength holes in metals [4], led to the field of plasmonics. More recently, much of the attention has been focused on sub-diffraction-limited “localized” modes confined in all three dimensions and “propagating” modes that are confined in two dimensions and propagate along the third axis in nanostructures incorporating metal/dielectric interfaces. The rich physics associated with surface plasmons and their potential for manipulating light at the nanoscale initiated the fields of nanophotonics [5] and metamaterials [6]. Plasmonics research has led to many advancements such as improved chemical detection [7–10] and enhanced quantum efficiency for detectors in the ultraviolet (UV), visible (vis) and near-infrared (NIR) spectral ranges [11–16]. However, while significant effort has been directed toward plasmonics, its promise for many applications has not been realized due to the high optical losses inherent in metals at optical frequencies [17–19]. Furthermore, while metal-based plasmonics has been successfully demonstrated in the UV to NIR spectral range, the very large negative permittivity at longer wavelengths limits its usefulness beyond the NIR. These issues have initiated a wide array of research into alternative, low-loss optical materials capable of supporting plasmon-like modes and/or exhibiting optical properties conducive to sub-diffraction confinement in the IR to terahertz (THz) spectral ranges [17–25].

The search for alternative materials for nanophotonic and metamaterial applications can be broken into two major research thrusts: 1) identifying novel, lower-loss, free-carrier-based plasmonic materials and 2)

exploring the use of dielectric materials. In the case of the former, efforts have focused on metal alloys [26–28], highly doped semiconductors [29–33] and more recently, graphene [34–40]. While the spectral range for localized plasmonic modes has been successfully pushed into the infrared using such materials, the plasmonic origin of the modes implies that they are still limited by the relatively fast electron/plasma scattering (typically on the order of 10–100 fs) [41–43]. On the other hand, the use of dielectric materials can dramatically reduce optical losses [44–50], but resonators with sub-diffraction optical confinement cannot be achieved using positive permittivity materials.

In contrast, *polar* dielectrics offer an opportunity to simultaneously achieve sub-diffraction confinement, low optical losses *and* operation in the mid-IR to THz spectral ranges through the stimulation of surface phonon polariton (SPhP) modes. These wavelengths offer a wealth of potential applications, for instance, the mid-IR features an atmospheric window between 8 and 12 μm where imaging through atmospheric obscurants and free space optics are highly desirable. This spectral window also coincides with a number of IR active vibrational fingerprints for the identification of trace levels of chemical species. Furthermore, blackbody emission peaks in this spectral range, making it a focal point for IR sources, imagers and detectors. On the long-wavelength side, the THz range exhibits a corresponding wealth of molecular rotational transitions and has been demonstrated to provide imaging through opaque objects. However, most of these potential applications have been limited by poor efficiencies, the requirement of cryogenic cooling, and/or by inefficient or the complete absence of monochromatic, coherent sources. Similar to efforts with plasmonic materials in the UV-Vis range, the high local electromagnetic fields and large potential Purcell factors from SPhP systems [23] should provide direct avenues towards enhancing these optical processes and thus enabling the next generation of optical devices. Prior work has also demonstrated that tailored thermal emission from SPhP modes within sub-wavelength SiC wires provided polarized, narrow-band sources [51].

SPhPs are the result of polar optical phonons interacting with long-wavelength incident fields from the mid-IR (e.g., hexagonal BN [52–55] and SiC [20, 23, 56, 57]) to <10 THz (e.g., GaAs [58, 59], InP [60] and CaF_2 [61]), creating a surface excitation mediated by the atomic vibrations. Such SPhP modes can be stimulated in polar dielectric crystals between the longitudinal (*LO*) and transverse optic (*TO*) phonon frequencies, with this spectral range referred to as the “Reststrahlen” band [60, 62, 63]. In these materials, the mechanisms governing optical loss are derived

from the scattering of optical phonons, which typically occurs on time-scales in excess of a picosecond [60, 63]. This results in a drastic reduction in the optical losses of the SPhP modes [20, 23, 64] in comparison to their plasmonic counterparts [41–43]. With the recent advances in ultra high quality and/or purity materials such as SiC, III-V and III-nitride semiconductors, further reductions are anticipated. While significant efforts have been aimed at improving metal surfaces for plasmonics through template removal [65], epitaxial growth [66] and atomic layer deposition [8, 67, 68], the potential for improvement is even greater in crystalline dielectric and semiconductor materials as point and extended defect densities are reduced further [69–72]. Therefore high-quality polar dielectric crystals can provide low optical losses, and through modification of their crystal lattice properties offer a wealth of options for supporting localized, propagating and epsilon-near zero (ENZ) [73] SPhP modes over a broad and adaptable spectral range. As many of these materials can be epitaxially grown on other polar dielectric materials, SPhP devices operating at multiple frequencies are also possible [74, 75].

All of these advantages are coupled with the continuing developments in growth methods for various polar dielectric crystals and the realization of two-dimensional van der Waal’s crystals [76], such as hexagonal boron nitride (hBN). Such two-dimensional materials offer the potential for unanticipated optical properties. For instance, it was recently demonstrated [53, 54] that hBN is a naturally hyperbolic material [77], whereby a material exhibits metallic (negative) and dielectric (positive real permittivity) optical response along orthogonal principal axes [78–80]. Unlike plasmonic/dielectric hyperbolic metamaterials, hBN was shown to offer the potential to invert the sign of the permittivity along a given axis, while maintaining low optical losses and offer a one atom thick unit cell. Additionally, this inversion of the sign of the permittivity was also reported for $\text{SiO}_2/\text{SiC}/\text{SiO}_2$ SPhP-based metamaterial designs [81]. Further investigations into other polar dielectric van der Waals crystals [76] and polar dielectric crystals [77] should experimentally demonstrate a wealth of such low-loss, naturally hyperbolic materials as well as potentially uncover other unanticipated optical properties. Furthermore, these van der Waals crystals offer the exciting potential for realizing the fundamental limit in photon confinement of SPhP modes, with recent results demonstrating that SPhP modes can be supported within three monolayer thick hBN flakes [54] and in nanostructures $86\times$ smaller than the free-space wavelength [53]. Based on these observations, we propose that polar dielectric materials will provide the basis for realizing

low-loss metamaterials and nanophotonic devices in the mid-IR to THz spectral ranges.

Here we provide insight into the basic phenomena governing the Reststrahlen response that enables stimulation of SPhP modes; develop guidelines for identifying polar dielectrics with a high potential for nanophotonic applications; discuss the influence of various material properties upon their characteristics; and suggest directions for improved SPhP device performance through material and structural advancements over the state-of-the-art. Section 2 of this review will discuss the origins of the Reststrahlen band and the physical mechanisms behind SPhP modes. Section 3 provides a comparison of key SPhP materials spanning the mid-IR to THz spectral bands with both metal- and doped-semiconductor-based plasmonic materials. A review of recent advances in SPhP nanophotonic and metamaterial designs is also included. An overview of optic phonon dispersions and lifetimes, which define the operational frequency band(s) and influence the SPhP modal loss are presented in Section 4. These features are discussed in terms of fundamental lattice properties that include the interatomic bonding and masses of the lattice atoms. Finally, a brief perspective of the future potential of these materials for various applications and concluding remarks are provided in Section 5. A glossary of the various terms, acronyms and variables is also supplied.

2 The Reststrahlen band and surface phonon polaritons

In an effort to develop an understanding of SPhPs, it is instructive to begin with a review of the well-studied optical properties of metals and the SPPs they support. One such property is the high reflectivity that metals exhibit from the low (DC) to the high-frequency NIR-vis-UV regimes. The high reflectivity is derived from the ability of “free” or “unbound” electrons in metals to screen out incident optical fields. This makes possible the excitation of collective oscillations of the free carrier density, which are called plasmons. The interest in plasmons is demonstrated by the large, sustained and continually growing field of plasmonics [82–86].

When a plane wave is directed towards a metal surface with a frequency lower than the plasma frequency, ω_p , of the metal, free carriers begin to coherently oscillate in a direction opposing the incident electromagnetic (EM) field, as shown in the schematic in Figure 1A. This results in a negative real part $[\text{Re}(\epsilon)]$ of the permittivity (i.e., the

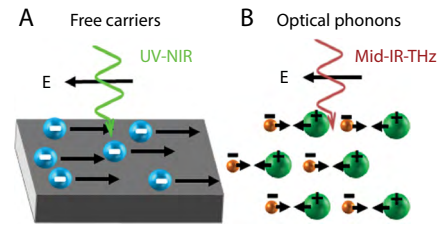


Figure 1 Schematic illustrating the collective oscillations of (A) free carriers in metals and (B) atomic displacements in the form of optical phonons in polar dielectrics that oppose incident radiation at frequencies below the plasma frequency of metals or between the longitudinal and transverse optical phonons in polar dielectrics. These oscillations are the foundations for the SPP and SPhP modes discussed in the text.

material does not “permit” the EM radiation), and an evanescent field inside the metal. The frequency dispersion of the permittivity far from interband transitions in metals is approximated by the modified Drude form:

$$\epsilon(\omega) = \epsilon_{\infty} - \frac{\omega_p^2}{\omega^2 + i\gamma\omega} \quad (2.1)$$

where ϵ_{∞} is the high-frequency permittivity of the material corresponding to the background from interband transitions, ω is the incident frequency, γ is the damping constant associated with the plasma oscillation, and $\omega_p = \sqrt{Ne^2 / (m^* \epsilon_0)}$, is the plasma frequency, where N , e , m^* and ϵ_0 are the free electron density, electron charge, effective mass of the carriers and the vacuum permittivity, respectively. Light scattering from metals can be governed by the excitation of bulk or surface plasmons. In particular, a spherical nanoparticle has a peak in the absorption cross-section when $\text{Re}(\epsilon) = -2$ [63] owing to a localized surface plasmon (LSP) resonance [87, 88]. The resonances also occur for non-spherical particles with geometrical factors determining the resonant values of $\text{Re}(\epsilon)$, which are on the order of unity for realistically attainable aspect ratios. This makes it difficult to fabricate metallic nanostructures supporting LSPs at wavelengths longer than the near-IR.

As mentioned above, a high reflectivity and negative $\text{Re}(\epsilon)$ are also observed for polar dielectric crystals within a spectral range referred to as the “Reststrahlen” band that gives rise to the SPhP phenomenon. The Reststrahlen band is bound by the *TO* and *LO* phonon frequencies. The two phonon modes correspond to out-of-phase atomic lattice vibrations with *k*-vectors aligned parallel (*LO*) and perpendicular (*TO*) to the incident field, with the positive (negative) charged lattice sites moving with (against) the direction of the field. As illustrated in Figure 1B,

this reflectivity arises from the coherent oscillations of the vibrating bound charges on the atomic lattice (optic phonons), which produce negative permittivities. The reflection spectra of a semi-insulating 4H-SiC substrate near the Reststrahlen band along with the corresponding Raman scattering spectra are presented in Figure 2A, to demonstrate the *TO* and *LO* phonon energies with respect to the Reststrahlen band. Analogous to metals, the dispersion relation can be approximated as a Lorentz oscillator for polar dielectric crystals:

$$\epsilon(\omega) = \epsilon_{\infty} \left(1 + \frac{\omega_{LO}^2 - \omega_{TO}^2}{\omega_{TO}^2 - \omega^2 - i\omega\gamma} \right) \quad (2.2)$$

with a pole at ω_{TO} , and a zero-point crossing at ω_{LO} , which are the *TO* and *LO* phonon frequencies, respectively. For a polar dielectric such as SiC, the permittivity is negative between ω_{TO} and ω_{LO} , and thus a plane wave in the material acquires an evanescent character. As such, both localized and propagating SPhP modes can be supported in nanostructures and on surfaces of polar dielectric crystals, respectively, analogous to LSPs and SPPs in metals. Alternatively, Eq. (2.2) can be expressed in terms of the high- (ϵ_{∞}) and low-frequency [$\epsilon(0)$] permittivities and/or the oscillator strength, [$s^2 = \omega_{TO}^2 (\epsilon(0) - \epsilon_{\infty})$]. Conversion is accomplished via the Lyddane-Sachs-Teller relation [60, 63]:

$$\left(\frac{\omega_{LO}}{\omega_{TO}} \right)^2 = \frac{\epsilon(0)}{\epsilon_{\infty}} \quad (2.3)$$

Additional information regarding the Reststrahlen phenomenon and the associated optical response can be found in the literature [60, 62, 63].

The values of the real and imaginary permittivity of a material can be obtained from experimental spectroscopic data, such as ellipsometry or reflection and transmission spectra, and if necessary, fitted to an analytic functional form such as Eq. (2.2). The spectral dependence of the permittivity calculated for a 4H-SiC epitaxial layer from infrared spectroscopic ellipsometry results reported by Tiwald et al. [57] are presented for the entire Reststrahlen band in Figure 3A, and a magnified view covering the range of $1 \geq \text{Re}(\epsilon) \geq -20$ is provided in Figure 3C. For comparison, Figure 3B and D give the corresponding plots for the lowest-loss plasmonic material, silver, using optical constants from both Palik's compendium (solid lines) [89] and Johnson and Christie (dashed lines) [90]. For the spectral range where localized modes can be supported in 4H-SiC and Ag, it is clear that the former exhibits values for $\text{Im}(\epsilon)$ that are significantly lower, in some cases reduced by more than an order of magnitude. Achieving such low values of $\text{Im}(\epsilon)$, where optical losses are lowest, is key to achieving the extremely narrow line-widths and high quality factors that were recently reported for SiC- [23, 64, 91] and hBN- based [53] localized SPhP nanoscale resonators. As will be discussed in Sections 3 and 5, the reduced $\text{Im}(\epsilon)$ has direct, positive implications for SPhP-based nano-optics.

The Reststrahlen response is at the heart of SPhP phenomena. Within this spectral band, the reflection of incident light approaches 100%, but unlike in metals, this is realized without free carriers. Therefore, one can think of these materials as "optical metals", which exhibit *optical* properties similar to those of metals below the plasma frequency, but with reduced damping rates and vastly different electrical properties. Similar to the case of SPPs,

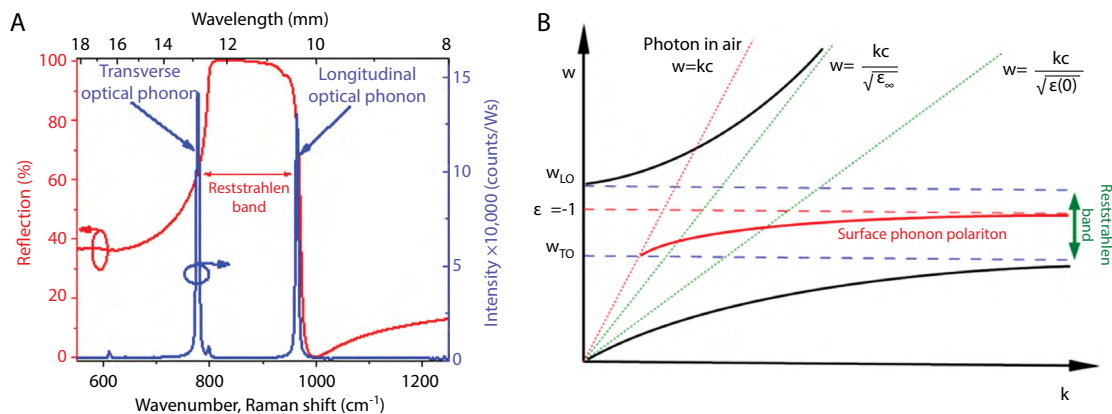


Figure 2 (A) FTIR Reflection (red trace) and Raman (blue trace) spectra collected from a semi-insulating 4H-silicon carbide wafer. (B) Phonon polariton dispersion curve for 4H-SiC for bulk (black lines) and surface (red line) phonon polaritons. The dashed horizontal lines correspond to the frequency locations of the LO and TO phonon frequencies. The dispersion of photons in air (red, dashed diagonal line) and in the high and low frequency limit of SiC (dashed green diagonal lines) are provided for comparison.

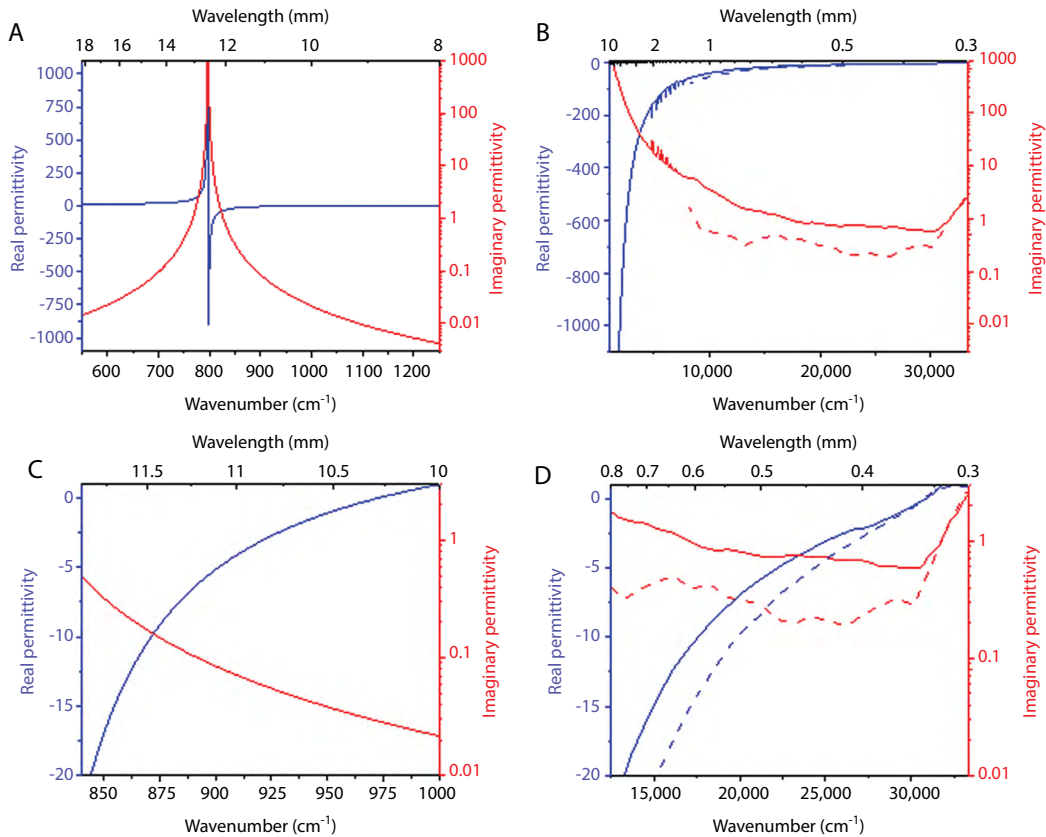


Figure 3 Real (blue) and Imaginary (red) permittivity (A) calculated for the 4H-SiC epitaxial layer from Ref. [57] and (B) of silver as calculated by Palik [89] (solid lines) and Johnson and Christie [90] (dashed lines). A magnified view of the spectral region where the $0 \geq \text{Re}(\epsilon) \geq -20$ is presented in (C) and (D), respectively.

there exists a momentum mismatch between the incident photons and the SPhP modes (illustrated for the 4H-SiC/air interface in Figure 2B along with the well-known bulk phonon polariton branches). This mismatch can be overcome using the coupling of the incident field to surface modes through a diffraction grating [92], high index prism [58, 93, 94], scattering from a nearby sub-wavelength particle such as an SNOM tip [20, 36, 38, 64] or via nanostructuring of the SPhP material into sub-wavelength particles [23, 53, 91]. By doing so, an overlap between the light line, $k=\omega/c$ and the SPhP dispersion curve,

$$k = \left(\frac{\omega}{c} \right) \sqrt{\frac{\epsilon_{\text{SPhP}} \epsilon_a}{\epsilon_{\text{SPhP}} + \epsilon_a}} \quad (2.4)$$

can be realized. Here, ϵ_{SPhP} and ϵ_a are the complex permittivity of the phonon-polariton material and the ambient medium, respectively. Once this momentum mismatch is overcome, the direct optical excitation of SPhP modes can be achieved and the promise of the materials can potentially be realized.

3 The promise of phonon polaritons: a comparison with plasmonics

The long lifetimes of phonon modes in bulk polar dielectrics appear promising from the viewpoint of realizing low-loss, sub-diffraction-limited optical modes using SPhP excitations. In this Section, we discuss the main characteristics of localized and propagating modes based on these excitations and compare them with the more completely explored case of plasmonic modes. In this context, we also provide an overview of some recent advances achieved using SPhP optical modes. Since a wide variety of geometries are possible, our first task is to define a few easy-to-use figures of merit (FOM) that can be employed to characterize and contrast both SPP and SPhP modes.

Localized modes. Calculation of the extinction, scattering and absorption cross-sections exhibit two distinct resonances for sub-diffraction SPhP spherical particles. The first occurs at $\omega < \omega_{\text{TO}}$, where the permittivity is

positive, and corresponds to a dielectric resonance supported by the enhancement of the refractive index near the TO phonon resonance [see Figure 3A] [95]. The second resonance is the dipolar localized SPhP mode and is the only resonance that exists regardless of how much the particle diameter is reduced. For a spherical nanoparticle with the permittivity described by Eq. (2.2), this “Fröhlich” mode [96] occurs at a frequency close to ω_{LO} , where $\text{Re}(\varepsilon) = -2\varepsilon_a$:

$$\omega_F = \sqrt{\frac{\omega_{LO}^2 + \frac{2\varepsilon_a}{\varepsilon_\infty} \omega_{TO}^2}{1 + 2\varepsilon_a / \varepsilon_\infty}} \quad (3.1)$$

Higher-order, non-radiative modes also exist in sub-wavelength spheres. In general, the resonance wavelength of the modes depends on the shape of the structure, but not on its dimensions as long as the enclosed volume is much smaller than the diffraction limit, $(\lambda_{res}/2n)^3$, where λ_{res} is the resonant wavelength, and $n = \sqrt{\varepsilon_a}$ is the index of refraction of the ambient medium.

It can be shown rigorously that the quality factor (Q) of an electrostatic mode is a function of the resonant wavelength, but is independent of the details of the geometry by which this resonance is realized [97]. Therefore, Q represents an excellent wavelength-dependent FOM for localized modes in both SPhP and plasmonic materials and can be estimated from the measured optical constants [97]:

$$Q = \frac{\omega \frac{d \text{Re}(\varepsilon)}{d\omega}}{2 \text{Im}(\varepsilon)} \approx \frac{\omega}{\gamma} \quad (3.2)$$

where the approximate equality is accurate for $\gamma \ll \omega_{LO} - \omega_{TO}$, and γ is the reciprocal of the SPhP lifetime near the zone center. Eq. (3.2) applies to both localized LSPs and SPhPs supported by materials with the permittivity described by Eqs. (2.1) or (2.2) for $\gamma \ll \omega$. Thus, one can quickly discern that reductions in optical losses lead to dramatic increases in Q . Note that Q in Eq. (3.2) does not take into account radiative coupling, important for larger nanoparticles [98], and should be considered as an upper bound for isolated particles. In addition, this also does not take into account near-field coupling [8, 99–101], Fano-interference [23, 102, 103] or other array-induced effects [99, 104–107] that can lead to increases in Q through coupling of extended modes, all of which are equally applicable to both SPhP and LSP modes.

In many cases, it is also of interest to have a FOM that evaluates the maximum electric-field enhancement $|E_{\max}|/|E_{\text{inc}}|$ possible for a particular geometry. This is a

complicated problem that has been explored for dimers and particle-plane combinations [100, 101, 108]. These structures may be used to localize electric fields over a tiny spatial region, with the ultimate $|E_{\max}|/|E_{\text{inc}}|$ only being properly derived using a nonlocal (rather than bulk) permittivity model. Since this topic falls outside the scope of this review, we will consider instead simple spherical particles, for which $|E_{\max}|/|E_{\text{inc}}|(\omega) \approx Q/(\omega d \text{Re}(\varepsilon)/d\omega) \approx 1/\text{Im}(\varepsilon)$ to a numerical factor of order unity. While $\text{Im}(\varepsilon)$ is often described as measuring “loss”, it can also justifiably represent a measure of field concentration. On the other hand, the normalized dispersion of the real part of the permittivity measures the ratio of the field energies residing inside and outside of the sub-wavelength structure:

$$\frac{U_{in}}{U_{out}} = \frac{\omega \frac{d \text{Re}(\varepsilon)}{d\omega}}{-\text{Re}(\varepsilon)} - 1 \quad (3.3)$$

Equipped with these FOMs for the localized modes, we can compare different SPhP-based and SPP-based materials. The Q [Eq. (3.2)] as a function of $\text{Re}(\varepsilon)$ is shown for the SPhP materials 4H-SiC [57] and GaAs [59], and the plasmonic materials n-type InGaAs [29], and silver [89, 90] in Figure 4A. A more comprehensive comparison of a wide range of plasmonic metals (red circles), metal alloys (pink hexagons), doped semiconductors (blue stars) and SPhP materials (green squares) are provided in Figure 4B. The corresponding numerical values are given in Tables 1 and 2 for LSP and SPhP materials, respectively. For noble-metal plasmonic structures, the electrostatic resonances tend to occur in the visible and near-IR, with Q in the 20–40 range, depending on the particular data set and material, corresponding to modal lifetimes on the order of 10 fs. In doped III-V semiconductors such as GaAs, InAs, and various alloys, the modal lifetime can be as long as 100 fs, but the typical operating wavelengths are near 10 μm [29, 118, 119]. As a result, no improvement in the Q over the metallic case is expected. Values of Q in the range of 2–6 have been calculated for n-InGaAs [29], with similar results observed for heavily doped wide-gap oxides and nitrides such as AZO [30, 31], GZO [32], ITO [30, 31], and TiN [26], with Q values on the order 10 [120]. However, recent work within n-type CdO demonstrates Q on the order of 40, similar to plasmonic metallic systems, while offering resonances in the mid-IR, thus providing a promising alternative plasmonic material [33].

For SPhP materials such as SiC, the damping time is increased to several picoseconds, while the operating frequency is reduced by an order of magnitude. The application of Eq. (3.2) gives maximum Q values >600 using the optical constants reported by Tiwald et al. [57], and

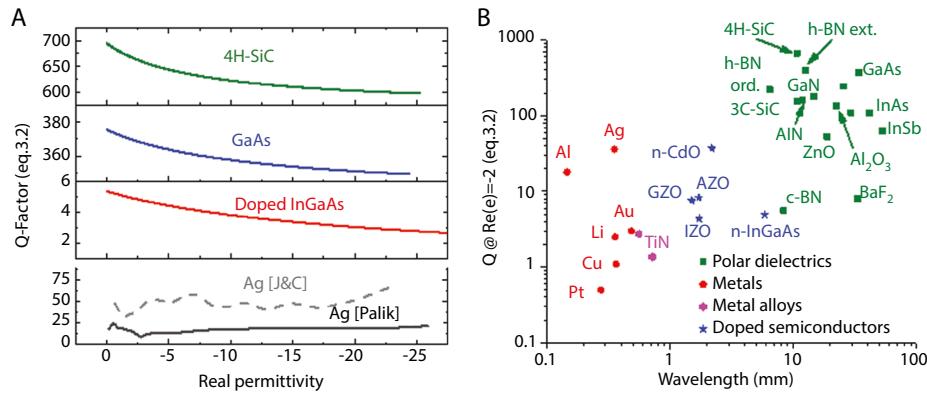


Figure 4 (A) calculated Q -factor [eq. (3.2)] for 4H-SiC (green trace) [57] and GaAs (blue trace) [59] SPhP and n-type $\text{In}_{0.3}\text{Ga}_{0.7}\text{As}$ (red trace) [29] and Ag [using optical constants from Palik (solid gray trace) [89] and Johnson and Christy (dashed light gray trace) [90]] SPP localized resonators as a function of $\text{Re}(\epsilon)$. (B) Comparison of Q for a spherical particle in air for all SPP and SPhP materials listed in Tables 1 and 2, respectively.

Table 1 Calculated wavelengths and corresponding localized, propagating and ENZ FOMs for plasmonic metals and doped semiconductors discussed in the text.

| Material | $\lambda[\text{Re}(\epsilon)=-2]$ (μm) | Q at $\text{Re}(\epsilon)=-2$ | $\lambda[\text{Prop.FOM}_{\text{max}}]$ (μm) | $\text{Prop. FOM}_{\text{max}}$ | $\lambda[\text{Re}(\epsilon)=0]$ (μm) | $\text{Im}(\epsilon) _{\text{Re}(\epsilon)=0}$ |
|---|---|---------------------------------|---|---------------------------------|--|--|
| | See eq. (3.2) | See eq. (3.2) | See eq. (3.4) | See eq. (3.4) | | |
| Metals (plasmonic) | | | | | | |
| Silver [90, 109] | 0.354 | 36 | 0.892 | 498 | 0.326 | 0.7 |
| Gold [89, 109] | 0.486 | 3 | 14.01 | 324 | 0.229 | 4.2 |
| Copper [89] | 0.365 | 1.1 | 6.89 | 101 | 0.155 | 2.2 |
| Aluminum [110] | 0.146 | 18 | 27.55 | 164 | 0.084 | 0.03 |
| Platinum [89] | 0.276 | 0.5 | 12.4 | 66 | 0.204 | 3.33 |
| Lithium [89] | 0.359 | 2.5 | 0.918 | 28 | 0.188 | 0.37 |
| TiN (800C) [26] | 0.56 | 2.74 | 2 ^a | 20 ^a | 0.51 | 2.9 |
| TiN (400C) [26] | 0.72 | 1.37 | 2 ^a | 7 ^a | 0.62 | 4.4 |
| Doped semiconductors (plasmonic) | | | | | | |
| Al:ZnO [30, 31] | 1.72 | 8.23 | 2 ^a | 7.6 ^a | 1.355 | 0.31 |
| Ga:ZnO [31, 32] | 1.5 | 7.56 | 2 ^a | 9.2 ^a | 1.18 | 0.347 |
| In:ZnO [31] | 1.73 | 4.35 | 2 ^a | 3.9 ^a | 1.39 | 0.688 |
| n-InGaAs [29] | 5.85 | 4.93 | 18.59 | 13.9 | 5.41 | 2.193 |
| n-CdO [33] | 2.18 | 37.1 | 16.39 | 97.8 | 1.87 | 0.127 |

^aSpectral range for optical constants limited to 2 μm and thus, propagating FOMs do not correspond to maximum values, only maximum values from reported results. All values were derived from references as noted in the table. Values were calculated using Eqs. (3.2), (3.4) and the value of $\text{Im}(\epsilon)$ at the ENZ point for the reported FOM values for localized, propagating and ENZ modes, respectively.

are consistent with values extracted from state-of-the-art substrates and epilayers that we have measured. Note that these values are over an order of magnitude higher than in noble metals. The maximum attainable Q is limited by the intrinsic damping due to phonon-phonon scattering, which is discussed in Section 4. In real structures, the imaginary part of the permittivity and, hence, the Q are also reduced by surface roughness in both plasmon-based and phonon-based structures. In addition, the Q of nanostructures from SPhP material may be affected by free carriers via the Drude term given in Eq (2.1), with their

presence of resulting in a blue-shift of the resonances and some reduction of the Q dependent upon the mobility of the free carriers, consistent with the influence of LO phonon-plasmon coupling upon the Raman spectra of polar semiconductors [121, 122].

At the Fröhlich resonance with $\text{Re}(\epsilon)=-2$, $\omega d\text{Re}(\epsilon)/d\omega \sim 10-30$ for both noble metals and doped semiconductors (with values ≈ 20 for Ag [90]), the permittivity dispersion is enhanced in SPhP materials. For 4H-SiC at $\lambda=10.7 \mu\text{m}$, $\omega d\text{Re}(\epsilon)/d\omega \approx 60$ [57], while for GaAs at $\lambda=34.6 \mu\text{m}$, $\omega d\text{Re}(\epsilon)/d\omega \approx 150$ [59]. From Eqs. (2.1) and (2.2), the

Table 2 *TO* and *LO* phonon frequencies reported in the specific reference, high and low-frequency permittivity, best reported damping constants and calculated wavelengths and corresponding localized, propagating and ENZ FOMs for phonon polariton materials discussed in the text.

| Material | ω_{TO} (cm ⁻¹) | ω_{LO} (cm ⁻¹) | $\lambda Re(\epsilon)=-2 $ (μm) | | Q at $Re(\epsilon)=-2$ | | $\lambda Prop. FOM _{max}$ (μm) | | $\lambda Re(\epsilon)=0 $ (μm) | | $Im(\epsilon) _{Re(\epsilon)=0}$ | |
|--|-----------------------------------|-----------------------------------|---------------------------------|---------------|--------------------------|---------------|---------------------------------|-----------------|--------------------------------|--|----------------------------------|--|
| | | | See eq. (3.2) | See eq. (3.2) | See eq. (3.2) | See eq. (3.4) | See eq. (3.4) | See eq. (3.4) | | | | |
| Polar dielectrics (phonon polariton) | | | | | | | | | | | | |
| h-BN ord. (ext.) [53] | 1360 (760) | 1614 (825) | 6.5 (12.5) | 221 (399) | 7 (12.9) | 54.3 (26.9) | 6.2 (12.1) | 0.07 (0.05) | | | | |
| c-BN [111] | 1070 | 1300 | 8.3 | 6 | 8.6 | 1 | 7.8 | 1.53 | | | | |
| 4H-SiC [57] | 797 | 973 | 10.7 | 668 | 11.9 | 220.3 | 10.3 | 0.07 | | | | |
| 3C-SiC [112] | 796.1 | 973 | 10.7 | 934 | 11.9 | 304.9 | 10.3 | 0.0199 | | | | |
| w-AlN [113] | 669 | 916.1 | 11.9 | 162 | 13.7 | 65.9 | 10.9 | 0.0479 | | | | |
| Al ₂ O ₃ ord. (ext) band 1 [114] | 633.6 (582.4) | 906.6 (881.1) | 11.9 (12.5) | 171 (251) | 15 (14) | 138.5 (80.9) | 10.5 (10.8) | 0.0272 (0.0173) | | | | |
| Al ₂ O ₃ ord. (ext) band 2 [114] | 610 | 888.9 | 12.4 | 120 | 14.7 | 59.4 | 11.3 | 0.0579 | | | | |
| w-GaN [115] | 569 (397.5) | 629.5 (510.9) | 17.3 (23.5) | 104 (82) | 17.5 (24.6) | 3.1 (13.3) | 17.3 (23.3) | 6.7 (1.075) | | | | |
| Al ₂ O ₃ ord. band 3 [114] | 537 | 732.5 | 14.6 | 180 | 17.1 | 80.8 | 13.6 | 0.06 | | | | |
| ZnO ord. (ext.) [116] | 439.1 | 481.7 | 22.3 | 136 | 22.6 | 6.9 | 22.2 | 1.65 | | | | |
| GaP [60] | 409.1 (380) | 588.3 (547.5) | 18.8 (19.4) | 53 (51) | 22 (23.3) | 23.8 (26.8) | 17 (17.4) | 0.12 (0.12) | | | | |
| AlAs [117] | 366.3 | 401.9 | 25.3 | 360 | 26.7 | 64.7 | 24.9 | 0.14 | | | | |
| InP [60] | 360.5 | 400.1 | 25.4 | 245 | 27 | 46.9 | 25 | 0.17 | | | | |
| GaAs [59] | 307.2 | 347.5 | 29.3 | 110 | 31.5 | 26.6 | 28.7 | 0.39 | | | | |
| InAs [60] | 270 | 300.3 | 33.9 | 370 | 36 | 83 | 33.3 | 0.15 | | | | |
| BaF ₂ [89] | 218.9 | 243.3 | 41.7 | 109 | 44.4 | 25.3 | 41.2 | 0.58 | | | | |
| InSb [60] | 217.8 | 388.1 | 33.3 | 8 | 50 | 6.2 | 26.7 | 0.22 | | | | |

All values were derived from references as noted in the table and are organized from highest energy *TO* phonon to lowest. Some materials, such as Al₂O₃, exhibit multiple Reststrahlen bands and these are labeled by the order of their relative energies. Materials such as hBN that exhibit significant anisotropies in the reported optical constants are reported for the ordinary and extraordinary principal axes. Values were calculated using Eqs. (3.2), (3.4) and the value of $Im(\epsilon)$ at the ENZ point for the reported FOM values for localized, propagating and ENZ modes, respectively. Note that the origin of the *LO* and *TO* frequencies in Table 2 and 3 from least-squares fitting to optical spectra and first principles calculations, respectively, do lead to some deviations between the results.

dispersion is enhanced by a factor of $\omega_{LO}/[2(\omega_{LO}-\omega_{TO})]$ in SPhP materials, particularly in those with less polar bonds and a small LO/TO splitting, such as GaAs (see Table 3). Using Eq. (3.3), we find that some SPhP materials have almost all of their energy residing in the structure rather than the surrounding medium. While an “ideal Drude” material with $\epsilon_\infty=1$, has $U_{in}=2U_{out}$, in isolated particles comprised of real metals or doped semiconductors, it is also the case that $U_{in}\gg U_{out}$.

The potential of localized SPhP resonant particles has been demonstrated in several works, starting with the first observations which occurred in the studies of interstellar SiC nanoparticles [123]. The first efforts focusing on the use of SPhP materials for realizing localized resonances took place in 2002 with the seminal works of Hillenbrand et al. [20] and Greffet et al. [124]. In the former, scanning near-field optical microscopy (SNOM) was performed on 4H-SiC surfaces, imaging the material-induced resonance from the image charge of the Pt-coated SNOM tip. As shown in Figure 5A, the 4H-SiC exhibits a dramatic enhancement in the scattering amplitude of the incident optical fields at the resonance frequency associated with the image charge of the SNOM tip in comparison to the

surrounding gold. Greffet et al. [124] demonstrated the first infrared perfect absorber, with coherent, polarized thermal emission (Figure 5B) that was maintained over many free-space wavelengths by writing a ruled grating into a SiC substrate. The high absorption cross-section of such sub-wavelength SPhP resonators is a driving force for many potential applications, including mid-IR narrow-band thermal emission sources with tailored spectral characteristics. This has led to many subsequent efforts, including the work of Schuller et al. [51], in which the thermal emission from sub-wavelength diameter SiC nanowires was demonstrated to provide polarization-dependent emission spectra that corresponded directly to the SPhP modes observed in the extinction spectra, as shown in Figure 5C. Such localized SPhP modes have been demonstrated to provide enhanced chemical spectroscopy through the surface-enhanced infrared absorption (SEIRA) of anthracene using spherical particles of 3C-SiC and Al_2O_3 [125].

More recently, localized SPhP modes have again become an exciting area of research. In the past year, two articles appeared demonstrating experimental Q's from SPhP resonances well-beyond the theoretical limit

Table 3 Isotope averaged atomic masses and reduced effective charges (Z) are given for a variety of materials.

| Material | $m_1(m_2)$ (amu) | $ Z $ | $\omega_{LA}(X)$ ($\omega_{TO}(X)$) (cm ⁻¹) | $\omega_{TO}(\Gamma)$ ($\omega_{LO}(\Gamma)$) (cm ⁻¹) | Reststrahlen Bandwidth (cm ⁻¹) | $\tau_{TO}(\Gamma)$ ($\tau_{LO}(\Gamma)$) (ps) |
|----------|------------------|-------|---|---|--|--|
| Si | 28.09 (28.09) | 0 | 414 (414) | 520 (520) | – | 1.63 (1.63) |
| 3C-SiC | 28.09 (12.01) | 1.01 | 630 (751) | 784 (951) | 154 | 2.93 (1.53) |
| c-BN | 10.81 (14.01) | 0.88 | 921 (921) | 1057 (1284) | 227 | 5.95 (2.54) |
| BP | 10.81 (30.97) | 0.21 | 534 (727) | 821 (831) | 10 | 2.11 (2.18) |
| BAAs | 10.81 (74.92) | 0.15 | 324 (634) | 700 (704) | 4 | 8776 (6425) |
| BSb | 10.81 (121.75) | 0.35 | 230 (560) | 604 (617) | 13 | 428.5 (217.4) |
| c-AlN | 26.98 (14.01) | 1.19 | 587 (654) | 650 (901) | 251 | 2.89 (0.87) |
| w-AlN | 26.98 (14.01) | 1.19 | 517 (630) ^a | 600 (911) ^b | 311 | 2.01 (0.88) ^b |
| c-GaN | 69.72 (14.01) | 1.13 | 354 (604) | 554 (737) | 183 | 0.55 (1.04) |
| w-GaN | 69.72 (14.01) | 1.12 | 317 (570) ^a | 534 (741) ^b | 207 | 0.64 (0.88) ^b |
| BeTe | 9.01 (127.60) | 0.47 | 160 (424) | 467 (500) | 33 | 65.91 (17.39) |
| LiF | 6.94 (19.00) | 0.72 | 357 (357) | 320 (654) | 334 | 1.07 (0.24) |
| AlSb | 26.98 (121.75) | 0.53 | 150 (287) | 314 (330) | 16 | 360.1 (98.21) |
| GaAs | 69.72 (74.92) | 0.56 | 223 (244) | 274 (294) | 20 | 3.46 (2.68) |
| InP | 114.82 (30.97) | 0.65 | 183 (317) | 317 (340) | 23 | 5.30 (58.56) |
| InAs | 114.82 (74.92) | 0.6 | 177 (200) | 227 (244) | 17 | 1.38 (40.65) |
| InSb | 114.82 (121.75) | 0.41 | 143 (153) | 183 (190) | 7 | 2.72 (2.96) |

Here, m_1 is the mass of the first atom in each binary material listed in the first column, and m_2 is the mass of the second atom. Also given are the calculated phonon frequencies for the LA and TO branches at the X point. The frequency difference, $\omega_{TO}(X)-\omega_{LA}(X)$, gives a measure of the $A-O$ gap and is directly related to the mass difference of the constituent atoms. The calculated phonon frequencies for the TO and LO branches at the Γ point are given. This frequency difference, (Reststrahlen bandwidth), gives a measure of the LO/TO splitting and is correlated with the reduced effective charges. The calculated intrinsic, room-temperature bulk optic phonon lifetimes near the Γ point and the Reststrahlen band as measured by the LO and TO frequencies at the Γ point are also given.

^aFor wurtzite structures the highest acoustic (lowest optic) frequencies at the M point are given.

^bFor wurtzite structures the lowest (highest) frequency optic modes at the Γ point are given, as well as their corresponding lifetimes.

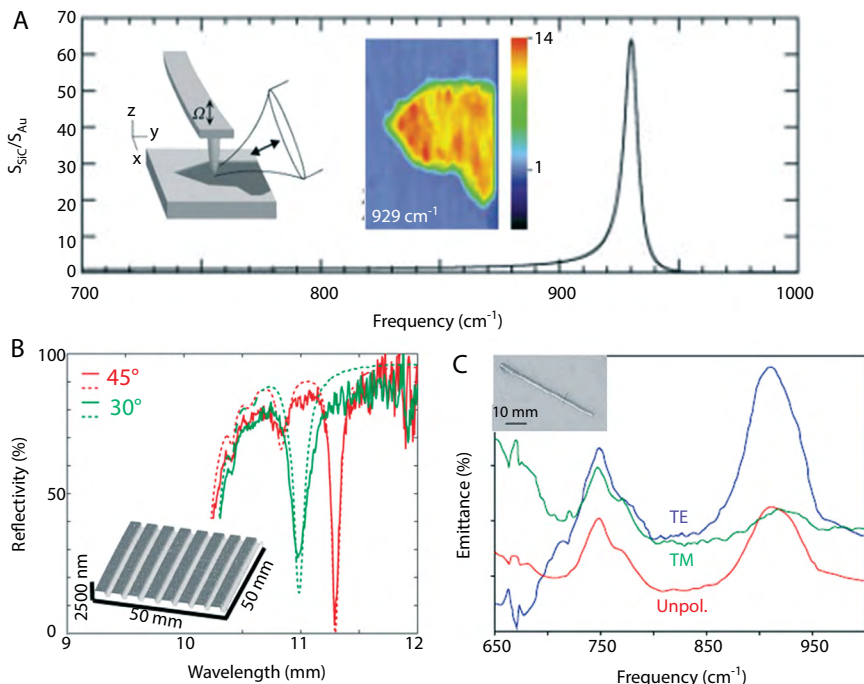


Figure 5 (A) Enhanced scattering spectrum of a SiC surface with respect to the surround gold surface within the mid-IR. Inset: schematic of the SNOM experimental setup and corresponding SNOM spatial plot. The Au and SiC surfaces exhibit low (blue) and high (yellow/red) scattering intensities within the plot. (B) Angle dependence of the reflectivity of SiC gratings within the Reststrahlen band demonstrating the ultranarrow and polarization sensitive SPHP response. Inset: AFM micrograph of SiC grating. (C) Polarized Mid-IR thermal emittance spectra of SiC whisker (inset). Reproduced with permission from Ref. [20] (A) [124], (B) and [51] (C).

for plasmonic nanoparticles. The first effort, reported by our group [23] showed that lithographic fabrication could be used to design SPHP resonators with *a priori* defined resonant frequencies, accomplished through the control and design of nanostructure geometry, size and periodicity (Figure 6A). The resonances exhibited up to 90% absorption of the incident light, with exceptionally narrow linewidths (7–25 cm⁻¹), which correspond to exceptionally high Q factors, (45–135). More

recent efforts within our group have demonstrated Q’s in excess of 250 and resonance tunability over the entire Reststrahlen band via changes in nanostructure size [23, 91], shape and periodicity [91]. Furthermore, it was demonstrated that the broad tunability of the monopolar resonances could be achieved by varying the pitch, corresponding to changes in filling fraction of 20%–2%, yet these spectral shifts were observed with minimal reduction in the resonance amplitude [91]. Efforts by

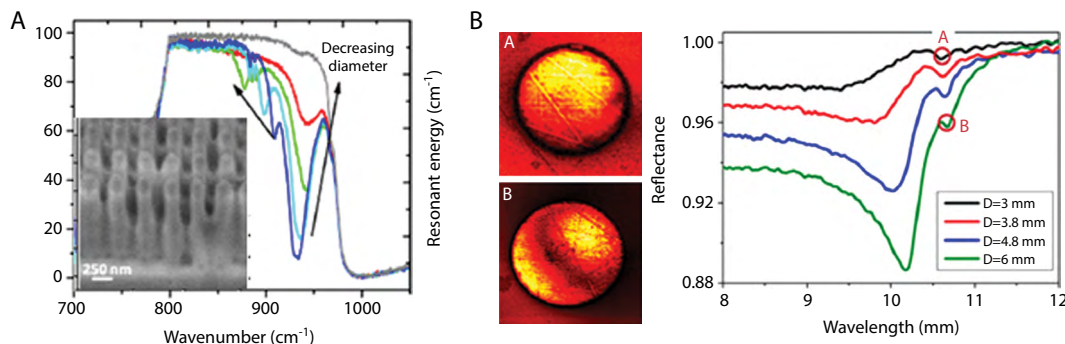


Figure 6 (A) Experimental FTIR reflection spectra of localized SPHP resonances in periodic arrays of 6H-SiC nanopillar arrays with varying diameters. Inset: SEM micrograph of representative nanopillar array. (B) SNOM images of SiC through circular gold apertures and the corresponding FTIR reflection spectra. Reproduced with permission from Ref. [23] (A) and [64] (B).

Wang et al. [64] reported similarly high Q -factors, with values >60 , using SNOM investigations of SiC substrates through defined circular apertures in a metal surface as shown in Figure 6B. Such high- Q localized SPhP modes also provide interesting optical interference effects, such as those between the bulk LO phonons and the localized SPhP modes of SiC nanopillars (see Supplementary Material from Ref. [23]). Such effects enable the investigation of Fano and other interference phenomena and the associated dark modes which typically exhibit exceptionally narrow linewidths [102]. These high Q -factors were also observed with field enhancements (E^2) in excess of $5000\times$ for SiC nanopillars [23], which is on par with or better than values observed within plasmonic nanostructures. Such large enhancements demonstrate the potential for such systems to enhance local emitters or IR-active vibrational modes for molecular spectroscopy. While higher enhancements have been reported for near-field coupled nanoparticles via plasmonic “hot-spot” formation [8, 100, 101], similar effects are anticipated within SPhP structures. However, this behavior has not yet been explored in any depth, so comparisons of such coupled structures are premature.

Recently, SPhP modes within hexagonal boron nitride (hBN) demonstrated another possibility for polar dielectrics unavailable in plasmonic systems: natural hyperbolic optical response [53, 54]. By definition a hyperbolic material is one in which the real permittivities along the two orthogonal principal axes have opposite signs, (i.e. the principal axes exhibit metallic and dielectric like optical behavior simultaneously) and is the basis of many efforts in super-resolution imaging, quantum nanophotonics or fluorescence engineering [53, 54]. Nanostructures of hBN on quartz were shown to exhibit similarly high Q -factors (60–280) as those observed in SiC systems, except they were observed within two distinct spectral bands corresponding to the upper (6.2–7.3 μm) and lower (12.1–12.8 μm) Reststrahlen bands. Furthermore, the resonances implied the presence of a novel type of optical mode, the hyperbolic polariton [53]. Such hyperbolic polaritons offer sub-diffraction confinement, with the mode confined within the volume of the material, rather than on the surface. SNOM-based measurements enabled the extraction of the SPhP dispersion relationship within hBN flakes, and they demonstrated the potential to support such modes in flakes as thin as three atomic layers (~ 1 nm) [54]. Such efforts illustrate the immense potential of SPhP materials and can provide the building blocks for a wide array of potential metamaterial and nanophotonic applications, as will be discussed in Section 5.

Propagating modes. Numerous potential geometries for propagating polariton modes can be envisioned. While it is often said that metal-based SPPs are very weakly confined at the wavelengths where SPhP modes are supported, the confinement can be arbitrarily strong at any wavelength for the so-called MIM (metal-insulator-metal) waveguide with very thin insulator layers and various geometries. Thus, building on the previous work for single interface SPPs [126], we employ a FOM that represents the ratio of the propagation length L_p to the vertical extent L_m (confinement of field orthogonal to propagation direction) of the mode at the vacuum/negative-permittivity material interface, since we consider this to be the best single-parameter measure of the “usefulness” of the propagating polariton mode. We normalize the propagation length to λ , and the modal extent to the “diffraction-limited” value of $\lambda/2$. Therefore, the FOM can be thought of as quantifying the L_p for a given L_m .

To simplify the expression, we assume further that $\text{Re}(\epsilon) \ll -1$ and neglect the penetration of the mode into the negative-permittivity material. Therefore, the FOM for such propagating modes represents an upper bound on the $L_p/2L_m$ quantity for simple polariton modes, but our empirical work shows it to be applicable to the MIM and other 1D geometries. If the surrounding medium has a refractive index larger than 1, $L_p/2L_m$ is reduced, which confirms its status as the upper bound. When the modal area is normalized to $(\lambda/2)^2$, the FOM appears to describe well the ratio of the normalized propagation length to the normalized modal area for 2D modes [127], although establishing the generality of this upper bound is beyond the scope of this review. From this, it is straightforward to show that:

$$FOM = \frac{L_p / \lambda}{2L_m / \lambda} = \frac{|\text{Re}(\epsilon)|^{3/2}}{\text{Im}(\epsilon)} \quad (3.4)$$

While Eq. (3.4) is suitable for comparing various sets of measured optical constants, further insight is gained by re-expressing the FOM in terms of the frequencies and damping rates for SPP and SPhP materials using Eqs. (2.1) and (2.2):

$$FOM_{SPP} = \frac{\left(\epsilon_\infty - \frac{\omega_p^2}{\omega^2}\right)^{3/2} \omega^3}{\gamma \omega_p^2} \approx \frac{\omega_p}{\gamma} \quad (3.5)$$

as the value that is asymptotically approached in the long-wavelength limit.

For SPhP modes, the FOM is a strong function of wavelength described by the following expression:

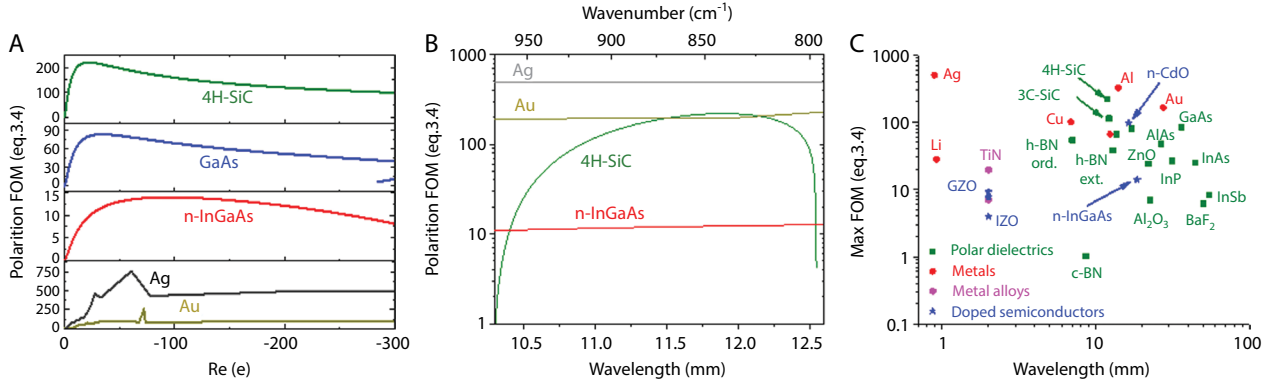


Figure 7 (A) Calculated FOM for propagating polariton modes [eq. (3.4)] for 4H-SiC (green trace) [57] and GaAs (blue trace) [59] SPhP and n-type $\text{In}_{0.3}\text{Ga}_{0.7}\text{As}$ (red trace) [29], Ag (gray trace, using combined optical constants from Johnson and Christy [90] with Bennett and Bennett [128]) and Au (yellow trace, using combined optical constants from Palik [89] and Ordal [109]) SPP propagating modes as a function of $\text{Re}(\epsilon)$. (B) Comparison of calculated propagating polariton FOM for 4H-SiC, n-type $\text{In}_{0.3}\text{Ga}_{0.7}\text{As}$, Ag and Au over the spectral band corresponding to the Reststrahlen band of 4H-SiC (10.3–12.5 μm). (C) Comparison of calculated propagating polariton FOM for all SPP and SPhP materials listed in Tables 1 and 2, respectively.

$$FOM_{\text{SPhP}} \approx \frac{\sqrt{\epsilon_{\infty}} (\omega_{\text{LO}}^2 - \omega^2)^{3/2} (\omega^2 - \omega_{\text{TO}}^2)^{1/2}}{\gamma \omega (\omega_{\text{LO}}^2 - \omega_{\text{TO}}^2)} \quad (3.6)$$

with the maximum occurring at

$$\omega_o = \omega_{\text{TO}} \sqrt{\frac{1 + \sqrt{1 + 3 \left(\frac{\omega_{\text{LO}}}{\omega_{\text{TO}}}\right)^2}}{3}} \approx \frac{3\omega_{\text{TO}} + \omega_{\text{LO}}}{4} \quad (3.7)$$

corresponding to a FOM value:

$$FOM_{\text{SPhP}} \Big|_{\omega_o} \approx \frac{3\sqrt{3}\omega_{\text{TO}}\sqrt{\epsilon_{\infty}}}{16\gamma} \left[\left(\frac{\omega_{\text{LO}}}{\omega_{\text{TO}}}\right)^2 - 1 \right] \quad (3.8)$$

The FOMs for 4H-SiC, GaAs, n-InGaAs, silver and gold are given as a function of $\text{Re}(\epsilon)$ in Figure 7A and clearly demonstrate that while SPhP materials can provide significant advantages for localized resonators, noble metals can offer similar if not higher FOMs for propagating modes when one considers systems where MIM-type structures can be used to enforce arbitrary z-confinement. This is further demonstrated for Ag, Au, n-InGaAs and 4H-SiC over the mid-IR Reststrahlen band of 4H-SiC in Figure 7B. Note that in the case of both silver and gold, no one data set covers the entire spectral range and thus for this comparison a combination of the Johnson and Christy [90] and Bennett and Bennett [128] datasets were used for silver, while a combination of the Palik [89] and Ordal [109] datasets were used for gold. Over this spectral range, 4H-SiC is competitive with the noble metals, but does not display

a significant advantage when MIM-type geometries are employed for SPP systems. A comparison of a wide array of plasmonic metals, doped-semiconductors¹ and SPhP materials are provided in Figure 7C, with the corresponding maximum FOM values provided in Tables 1 and 2, respectively. For noble metals, the FOM for SPP modes exceeds the Q as $\omega_p > \omega$, and the presence of interband transitions in metals is not a significant factor at longer wavelengths. In heavily-doped, wide-gap semiconductors, $\gamma \sim 0.05\text{--}0.1$ eV at best, which leads to values that are generally lower than in noble metals (or comparable in the case of TiN) [27, 120]. However, forthcoming results from n-type CdO are very promising with propagating FOMs on par with noble metals in the mid-IR [32]. The reduction in the FOM for propagating modes in SPhP materials can be understood by considering that while these materials have longer lifetimes and therefore lower damping, they also exhibit significantly reduced group velocities, v_g due to their strong dispersion. Therefore, the corresponding polariton decay length $L^{\perp} \sim \gamma/v_g$ is comparable or shorter than noble metals.

Since the SPhP FOM does not exceed that of noble metals, the main reason to employ SPhP waveguides is to eliminate complexity of the MIM and similar structures needed to obtain sub-diffraction-limited L_m rather than to improve the propagation length (for the same degree of confinement). It may also be convenient in many cases to dispense with the use of noble-metal layers during the fabrication process and replace those with semiconductor

¹ Note: Optical constants for doped ZnO are currently only available out to 2 μm.

or dielectric materials (e.g., CMOS compatibility). Finally, some niche applications may arise where coupled waveguides and localized resonators are needed, for instance in nanophotonic circuit designs, whereby incorporating a single material for both the waveguides and the resonators may be beneficial and thus be aided through the use of SPhP materials.

While direct SPhP waveguides for improving the polariton propagation length may not appear to be an area of high potential payoff, the work on propagating SPhP-based waveguides and metamaterial designs is still of significant interest. In addition to the specific applications noted above, propagating SPhP modes can form the basis for a wide array of other applications such as integrated THz generation or stimulated Raman amplification for potential THz or infrared sources. Initial investigations into such applications were recently reported by Holmstrom et al. [129], who reported suspended waveguides

fabricated from n-type InP on InGaAs, with the resulting structure shown in Figure 8A. The authors characterized the confinement of propagating polariton modes using Raman scattering. Furthermore, Huber et al. [92] demonstrated the focusing of propagating SPhP modes onto a SiC surface using a simple, concave, gold focusing element as shown in Figure 8B. Such sub-diffraction focusing demonstrates the capability of manipulating the propagating SPhP modes on the nanoscale, of much importance for nanophotonic applications. Additional advantages can be found in the fabrication of extraordinary transmission (EOT) gratings, such as those reported by Urzhumov et al. [130]. As demonstrated in Figure 8C, the structural integrity of polar dielectric materials enables the fabrication and characterization of thin perforated membranes, with the resonance modes exhibiting both local and propagating properties with distinct polarization sensitivity. Finally, it was recently reported that both localized and

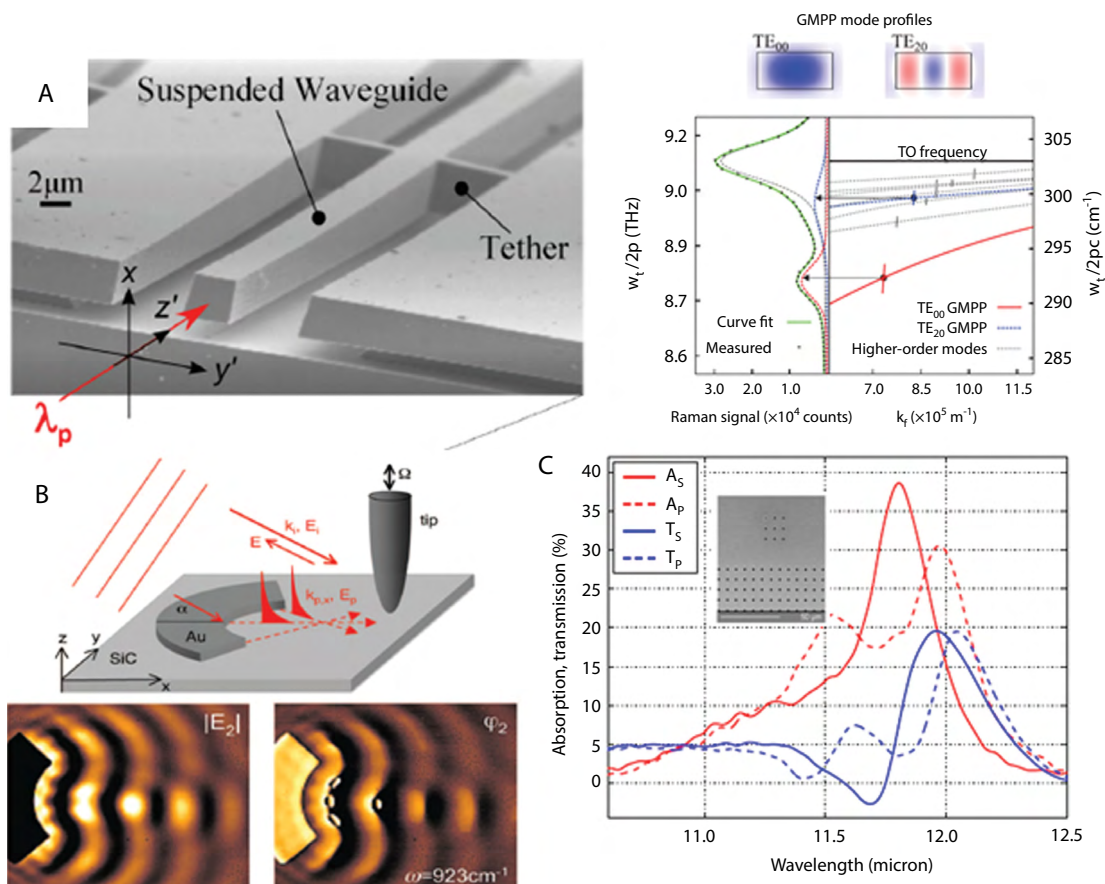


Figure 8 (A) SEM image of a n-InP suspended waveguide on InGaAs along with the corresponding calculated 9 THz TE_{00} (red solid curve), TE_{20} (blue dashed curve) and higher order waveguide modes (gray dotted curve) and corresponding Raman spectra (dots). (B) Schematic of the experimental SNOM apparatus used to demonstrate the focusing of propagating SPhP modes. The corresponding SNOM amplitude $|E_2|$ and phase (φ_2) images are provided below the schematic. (C) Experimental s- (solid lines) and p-polarized (dashed lines) absorption (red curve) and transmission (blue curve) spectra for an extraordinary optical transmission grating made of a perforated SiC membrane. Inset: SEM micrograph of representative structures. Reproduced with permission from Ref. [129] (A), [92] (B), and [130] (C).

propagating SPhP modes provide over an order of magnitude stronger optical forces with respect to metal-based plasmonic systems of the same geometry [131]. These results also demonstrate that when combined with the mechanical hardness of polar dielectric crystals, SPhP modes offer key advantages for optomechanical devices in the IR and THz spectral ranges as well. The hyperbolic polaritons observed within hBN also demonstrate the potential for novel propagating mode systems that may provide distinct advantages over SPP-based MIM counterparts. Due to the low-loss and volume-bound nature of the modes, it is possible that the sub-diffraction equivalent of an optical fiber could be realized [53], by which arbitrary z-confinement could be achieved via the physical size of the structure. Such modes could revolutionize nanophotonic waveguides for communications or photonic circuits, among other applications. However, in depth theoretical descriptions of these modes and experimental characterization of such systems are still lacking.

An additional type of propagating mode was originally predicted by Silveirinha and Engheta [73], whereby the propagation of a displacement current in air or other dielectric material could be realized, provided the medium is surrounded by another material with $\text{Re}(\epsilon) \approx 0$. Such epsilon near zero (ENZ) response can be found in plasmonic materials at a frequency somewhat lower than ω_p and SPhP materials at $\omega \sim \omega_{LO}$. For these ENZ ($\text{Re}(\epsilon) \sim 0$) structures that have drawn much recent interest, an important FOM is the magnitude of $\text{Im}(\epsilon)$ at the frequency for which $\text{Re}(\epsilon) = 0$. Using Eq. (2.2) for SPhP materials, we obtain $\text{Im}(\epsilon)|_{\text{Re}(\epsilon)=0} \approx \epsilon_\infty \gamma / [2(\omega_{LO} - \omega_{TO})]$. The behavior is similar to that described earlier in the context of localized resonances, as more strongly polar materials with low damping are expected to have the best characteristics. For 4H-SiC, the measured values are in the 0.028–0.129 [56, 57] range, as compared to 0.3 [90]–1.8 [89] for silver and 3.4 [90]–4.3 [89] for gold. For doped semiconductors that are reasonably well described by the Drude formula Eq. (2.1), $\text{Im}(\epsilon)|_{\text{Re}(\epsilon)=0} \approx \epsilon_\infty^{3/2} \gamma / \omega_p$, the values observed are comparable to those in metals [$\text{Im}(\epsilon)|_{\text{Re}(\epsilon)=0} \approx 2.2$ for n-InGaAs] [29].

While the mathematical formalisms associated with SPhPs and SPPs are similar, the difference in the origin of the two phenomena implies that they are fundamentally dependent upon distinctly different material properties. For instance, since SPPs are derived from free-carrier oscillations, the role of interband transitions and crystal properties is only secondary. In contrast, the SPhP modes intimately depend on the crystal lattice that supports them. Therefore, changes in the atomic masses, the interatomic bonding, the crystal structure and the incorporation of impurities and/or extended crystalline defects can

modify the Reststrahlen band. This leads to controllable changes in SPhP properties of polar dielectric materials, including the operational frequency, bandwidth and modal lifetimes (i.e., optical losses). It is therefore of critical importance to gain an understanding of how various crystal properties impact the optical response of the material, especially in the context of finding the highest-performing SPhP materials, those that are most degraded by poor crystal quality (and, therefore, with the greatest chance of improvement), and finally those operating in a spectral range well suited for a given application. In an effort to provide a degree of insight, we address these issues in more detail in Section 4.

4 Lattice properties and optic phonons: dispersion, lifetimes and SPhP modes

The characteristics of SPPs and SPhPs are generally discussed in terms of equations like Eqs. (2.1) and (2.2), respectively. These are well-known continuum forms for the dielectric functions for bulk systems, and for consistency, bulk values of the parameters are typically used. They are appropriate for SPPs and SPhPs that have spatial variations that are slow on the scale of the lattice constant, which is satisfactory except in the cases of extreme optical confinement.

The frequencies of bulk phonon modes, $\omega_j(\vec{q})$, are determined by such properties as the atomic masses, bonding, and crystal structures. These phonon frequencies are what determine the operational frequency range and bandwidth for the SPhP modes within a given material. Here, \vec{q} is the wavevector and j is the phonon branch index: *TO*, *LO* or acoustic (*A*) and the optical losses of SPhP modes are given by phonon lifetimes, $\tau_j(\vec{q})$. In most non-metallic materials near room temperature the phonon lifetimes are determined by intrinsic three-phonon scattering processes arising from crystal anharmonicity and by scattering from inhomogeneous distributions of the natural variations in the nuclear isotopes that occur in many of these materials. These processes provide an estimate of the upper bound on the phonon lifetime near room temperature and therefore should also provide a similar upper bound on the SPhP modal lifetimes, while the corresponding trends with crystal properties are reflected in both the optical phonon and the SPhP modal lifetimes. In real materials, both lifetimes are expected to be reduced due to additional contributions from scattering by crystal

defects and interfaces which will be discussed at the end of this section.

Crystals with a diatomic unit cell (e.g., Si, GaAs, cubic 3C-SiC) have three optic phonon branches (one *LO* and two *TO*) at higher frequencies and three acoustic branches at lower frequencies. Figure 9 gives the phonon frequency versus scaled wave vector (i.e., the phonon dispersion) for 3C-SiC (polar material, right-hand side) compared to Si (purely covalent material, left-hand side) in the $\Gamma \rightarrow K \rightarrow X$ high symmetry direction as calculated from density functional perturbation theory [134]. For the present purposes, we will restrict these discussions to cubic crystal lattices, however, the general trends discussed are applicable to other crystal phases. We will focus below on the following key features: 1) the scale of the optic phonon frequencies, 2) the frequency gap between the *LO* and *TO* phonon branches (*LO/TO* splitting), and 3) the frequency gap between the *TO* and lower-lying acoustic branches (*A-O* gap).

Optic phonon frequencies: The Reststrahlen band defines the operational range for SPhP modes in polar dielectric crystals. Thus, an understanding of the lattice properties that modify these phonon frequencies is necessary both to understand the Reststrahlen phenomenon and to predict what materials will be best suited for a given spectral range. In general, strong interatomic bonding and light atomic masses lead to a high phonon

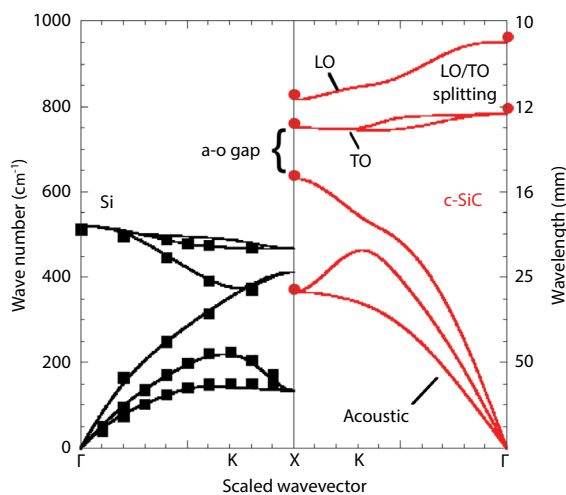


Figure 9 Calculated phonon dispersions in the $\Gamma \rightarrow K \rightarrow X$ high symmetry direction for Si (black curves) and 3C-SiC (red curves) with experimental data for Si (black squares) [132] and 3C-SiC (red circles) [133]. Polar 3C-SiC has a frequency gap between the acoustic and optic branches (*A-O* gap) and a frequency gap between the *LO* and *TO* branches (*LO/TO* splitting). These features are not present in Si, which has purely covalent bonding and identical unit cell atoms.

frequency scale, i.e., large acoustic phonon velocities and high frequency optic branches. For instance, 3C-SiC has a smaller unit cell mass and stronger bonding than does Si, which results in 50% higher optic phonon frequencies in 3C-SiC (see Figure 9). Therefore, to realize high-frequency SPhP response, lighter atomic masses and strong atomic bonding are required, with hBN offering the highest reported frequency response at $6.2\text{--}7.3\ \mu\text{m}$ ($1367\text{--}1610\ \text{cm}^{-1}$) for the upper Reststrahlen band [52–55].

It is instructive to consider the role that interatomic bonding and the individual atomic masses play using a simple diatomic linear chain model. This model consists of alternating atoms with different masses, m_{light} and m_{heavy} , interacting harmonically with spring constant, K , in a linear chain with periodic boundary conditions. The spring constant of this simple model is related to the set of harmonic interatomic force constants (IFCs) in real systems [135, 136]. The diatomic chain model supports two vibrational modes with frequencies [137]:

$$\omega_A = \sqrt{2K/m_{\text{heavy}}} \quad (\text{acoustic}) \quad \omega_{\text{Opt}} = \sqrt{2K/m_{\text{light}}} \quad (\text{optic}) \quad (4.1)$$

at the Brillouin zone boundary. It is apparent that larger K (stronger bonding) gives rise to both larger acoustic and optic phonon frequencies. This is illustrated for real systems in Figure 10, via the phonon dispersions of *c*-BN (right) and diamond (left). Despite having similar unit cell masses, the stronger bonding in diamond leads to a significantly larger phonon frequency scale, with *TO* phonon branches at $\sim 25\%$ higher frequency than in *c*-BN. This point is further highlighted by comparing the *TO* frequencies of *c*-BN and LiF (rock salt structure) given in Table 3. Due to the much stronger covalent bonding in *c*-BN, $\omega_{\text{TO}}(X)$ is more than two times larger than it is in LiF, despite having similar unit cell masses.

As demonstrated in Eq. (4.1), the optic and acoustic phonon frequencies depend inversely on the light and heavy atomic masses, respectively. In order to realize high frequency Reststrahlen bands and SPhP modes, polar dielectric crystals with small m_{light} are required, but m_{heavy} may be somewhat larger. However, as the difference in the atomic masses increases, the interatomic bond strength typically tends to decrease and thus reduces the Reststrahlen band frequency. Therefore, both properties must be taken into account in predicting operational frequency bands.

LO/TO splitting: In polar dielectric materials, long-range Coulomb forces contribute to increasing the *LO* to higher frequencies than the *TO* phonons, and result in a splitting of the *LO* and *TO* branches (*LO/TO* splitting). This is described by the Lyddane-Sachs-Teller relation [Eq.

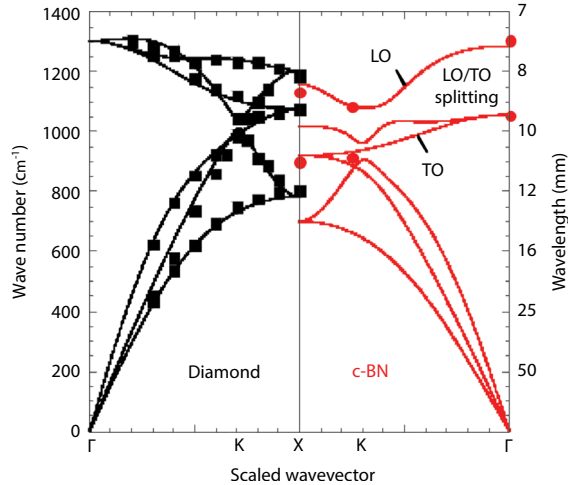


Figure 10 Calculated phonon dispersions in the $\Gamma \rightarrow K \rightarrow X$ high symmetry direction for diamond (black curves) and c-BN (red curves) with experimental data for diamond (black squares) [138] and c-BN (red circles) [139, 140]. c-BN has lower acoustic and TO frequencies than diamond due to weaker interatomic bonding, however, c-BN and diamond have similar LO frequencies due to the polar nature of the bonding in c-BN.

(2.3)], and can be seen in the phonon dispersions of 3C-SiC (Figure 9) and c-BN (Figure 10). The magnitude of this splitting gives the bandwidth of the Reststrahlen band and, therefore, the range over which SPhP modes can be supported. A measure of the polarity of the interatomic bonds, and therefore the LO/TO splitting, is given by the reduced effective charge, $Z = Z^* / \sqrt{\epsilon_\infty}$, [134] where, Z^* is the Born effective charge. The calculated Z and LO and TO frequencies at the Γ point for a number of materials are given in Table 3. Of these, c-BN, GaN and 3C-SiC have the largest reduced charges and, consequently, the widest LO/TO splittings, thus resulting in, the largest operational SPhP bandwidth.

Optic phonon lifetimes: It is the SPhP modal lifetime that governs optical losses of nanophotonic and metamaterial designs. This lifetime will depend on many aspects; both from intrinsic phonon-phonon scattering, as well as extrinsic effects (e.g., scattering from defects, impurities or surface damage) [135]. While both types of effects are active, the general trends associated with the former provide insight into the role that intrinsic crystal properties play in dictating this lifetime. While the SPhP modal lifetime is not equivalent to the bulk optic phonon lifetimes, the dependence of the latter upon various lattice parameters is reflected in the former as well. In fact, one can view the bulk optic phonon lifetimes at or near the Γ point, where coupling to optical fields is strong, as an approximate upper limit for SPhP modes.

In general, optic phonons in polar dielectric materials have longer lifetimes (~ 1 – 100 picoseconds) [60, 63] than free carriers in a metal (~ 10 femtoseconds) [41–43]. In many high-quality crystals at or above room temperature, intrinsic phonon-phonon scattering that arises from the anharmonicity of the crystal potential is the dominant mechanism limiting bulk phonon lifetimes. To lowest order in perturbation theory, scattering processes involve three phonons and their lifetimes depend inversely on the sum of all possible three-phonon scattering rates, $\Gamma_{\vec{q}_i, \vec{q}_j, \vec{q}_k}^{\vec{q}'', \vec{q}'}$, which are built from anharmonic matrix elements and the phonon frequencies [135, 141, 142]. The phonon lifetimes depend strongly on the available phase space for scattering, which is dictated by simultaneous conservation of energy and crystal momentum:

$$\omega_i(\vec{q}) \pm \omega_j(\vec{q}') = \omega_k(\vec{q}''); \quad \vec{q} \pm \vec{q}' = \vec{q}'' + \vec{G} \quad (4.2)$$

where \vec{G} is a reciprocal lattice vector. For materials in which the conservation conditions in Eq. (4.2) are difficult to satisfy, scattering of optic phonons is weak and the corresponding lifetimes are long. Though higher-order scattering processes are predicted to be significantly weaker than three-phonon processes [143, 144], they may become important for optic modes with severely restricted three-phonon phase space, especially at higher temperatures.

Optic phonon lifetimes have been determined from Raman scattering techniques for a number of materials (e.g., see Refs. [59, 60, 63, 145–155]), and first principles density functional theoretical methods have been developed and applied to calculate phonon dispersions and lifetimes without adjustable parameters (e.g., see Refs. [134, 141] and [156–158]). Here, we have used a first principles technique [159] to calculate and examine the near-zone-center optic phonon (TO and LO) intrinsic lifetimes, for the various polar dielectric materials given in Table 3. The calculated room-temperature bulk optical phonon lifetime reported here are in general accord with the available experimental data [56, 60, 63, 145–155], and fall in the range of 0.5 ps to 9 ns, orders of magnitude larger than SPP lifetimes. For instance, lifetimes between 0.6–0.8 ps and 1.4–1.9 ps were reported for wurtzite AlN [154] for the LO and TO phonon lifetimes, respectively, which compares quite favorably to our corresponding calculations of 0.88 and 2.01 ps. Similar agreement for other materials discussed here were typically found. A few notable exceptions, such as InP [150], were observed, however, in all cases both the experimental and calculated lifetimes were found to exceed reported plasmonic lifetimes [41, 42]. For

an estimate of the comparison between the optic phonon and the SPhP lifetimes in resonant nanostructures, our calculated values for 4H-SiC cylinders of various diameters are provided in Figure 11, demonstrating that the optic phonon lifetimes have an upper limit of roughly 3 ps. In comparison, SPhP lifetimes extracted from the resonance of the transverse dipolar and monopolar SPhP resonances observed within cylindrical 4H-SiC nanostructures presented in Figure 6A and Ref [23], were observed to fall in the range of 300–800 femtoseconds and appear to be relatively insensitive to the nanostructure diameter within this size range. For comparison, SPP lifetimes in Ag spheres as a function of diameter from Ref. [42] and the SPP lifetime ($1/\gamma$) for Ag extracted from Table 1 are also provided. Thus, SPhP modal lifetimes within a factor of 4–10 of the optic phonon values are observed, which is 1–2 orders of magnitude longer than the SPP modal lifetimes from Ag spherical particles. This is observed despite the possible damage to the surface of the SiC nanopillars via fabrication processes.

Certain trends can be seen in the lifetime data presented in Table 3. For instance, materials with a large mass difference between the constituent atoms tend to have larger optic phonon lifetimes, e.g., BAs, BSb, AlSb and BeTe. This trend is also observed in comparing $\tau_{LO}(\Gamma)$ of the InX materials (X=P, As, Sb), which demonstrate increasing LO lifetime with increasing anion mass (decreased mass difference). In addition, we find little difference in the optic phonon lifetimes between different lattice structures, cubic and wurtzite, for AlN and GaN.

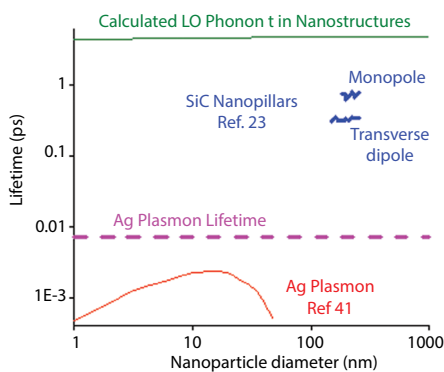


Figure 11 Calculated lifetimes for LO phonons within 4H-SiC nanostructures as a function of diameter (green trace) in comparison to values extracted from the resonance linewidths of SiC nanopillars reported by Caldwell et al. [23] (blue and light blue trace for modes as noted in figure). For comparison, the lifetimes of silver spherical particles are reported by Kreibig and Vollmer [42] (red trace) and extracted from the inverse of the damping constant for Ag are also provided.

The behavior of the optic phonon lifetimes can be largely understood in terms of the phonon dispersions and the conservation conditions [Eq. (4.2)], which give the phase space available for phonon-phonon scattering. It is convenient to characterize three-phonon scattering processes by the types of phonons involved, (e.g., the scattering of two optic phonons with an acoustic phonon is *OOA* scattering). There are three scattering channels that limit the intrinsic optic phonon lifetimes: i) *OOO*, ii) *OAA* and iii) *OOA*. In most materials, *OOO* scattering is forbidden by energy conservation, since the difference in energies of any two optic phonons is rarely as large as the energy of a third.

OAA scattering and the A-O frequency gap: In many materials, the decay of an optic phonon into two acoustic phonons (*OAA* scattering) is the dominant intrinsic scattering mechanism for optic phonons. However, this scattering can be severely restricted in polar materials that have a significant frequency gap between the acoustic and optic phonons, *A-O* gap (see Figure 9 for 3C-SiC). The origin of this *A-O* gap is readily seen from the solution of the diatomic linear chain model discussed above. As m_{light} decreases, the optic phonon frequency, ω_{opt} increases at the Brillouin zone boundary, and as m_{heavy} increases, the acoustic phonon frequency, ω_A decreases, thereby opening a frequency gap. Table 3 gives the isotope averaged atomic masses, m , and the frequencies of the highest acoustic (*LA*) and lowest optic (*TO*) phonons at the X point for a number of materials. The difference in these frequencies, $\omega_{TO}(X) - \omega_{LA}(X)$, gives a measure of the *A-O* gap in a material. As this gap increases, the conservation conditions [Eq. (4.2)], can severely restrict the phase space for *OAA* scattering, and in some materials prohibits this scattering altogether (e.g., AlSb, BAs, BSb, BeTe). Reduced *OAA* scattering gives significantly increased intrinsic optic phonon lifetimes in bulk crystals. Evidence for this can be observed in Table 3, where it is found that the longest optic phonon lifetimes correspond to materials with the largest mass differences between the constituent atoms. Because as the frequency of SPhP modes falls between ω_{TO} and ω_{LO} , the reduced *OAA* scattering is likely to be relevant for surface as well as bulk phonon modes.

The *A-O* gap is further increased for *LO* phonons in highly polar materials with strong Coulomb interactions between the ions, which gives higher *LO* frequencies. However, we note that this does not necessarily result in larger *LO* phonon lifetimes. For example, *c*-GaN has a large *A-O* gap and no *OAA* scattering for the zone center *LO* phonons. However, the *c*-GaN zone center *LO* lifetime is small, (~1 ps), compared to those of the other large mass difference materials in Table 3 (from 100's of ps). Large *LO/TO* splitting in GaN and in

other materials allows higher frequency acoustic phonons to participate in *OOA* processes, which normally play a lesser role in limiting optic phonon lifetimes than *OAA* scattering. For closely spaced optic branches (small *LO/TO* splitting), the conservation conditions limit *OOA* scattering to very low frequency acoustic phonons in a limited frequency window near the Γ point. However, in materials with limited *OAA* scattering (e.g., GaN), *OOA* scattering can be a particularly important mechanism.

Extrinsic defects: To this point, we have discussed only intrinsic phonon scattering, which gives the upper bound to the phonon lifetimes. In realistic materials, scattering by varying nuclear isotopes of a given atom [159, 160], impurities and extended defects can also limit optic phonon lifetimes [135]. However, extrinsic effects are system specific and difficult to generalize and therefore a detailed description of these effects is outside of the scope of this review. It is important to note that point and extended defects are expected to influence primarily the localized SPhP modes and result in lifetime reductions and resonance line broadening. These effects could be directly probed via sensitive near-field measurements (e.g., using SNOM) [25, 161, 162]. Such initial investigations were reported by Huber et al. [161] where modifications to the SNOM contrast were observed between crystal domains with the 4H- and 6H- stacking orders of SiC. However, such defects may also act as nanometer-scale sources of modified SPhP response that can be useful in the design of patterned nanophotonic or metamaterial devices. For instance, the incorporation of stacking faults in silicon carbide [69, 70, 163–173] could provide a means to modify the Reststrahlen band and, therefore, the SPhP response of specific nanostructures or nanophotonic/metamaterial designs. Experimental evidence for this were reported by Ocelic et al. [162] where it was demonstrated that the SPhP response could be severely damped via the patterned implantation of Be³⁺ ions into a SiC surface using ion beam implantation.

5 Realizing Mid-IR to THz nanophotonics and metamaterials: brief perspective

From the preceding Sections, it is apparent that SPhP materials can provide the basis for a wide array of potential nanophotonic or metamaterial applications. In particular, the dramatically higher *Q*'s exhibited by SPhP materials indicate the potential for high efficiency optical antennas suitable for enhancements of mid-IR emitters, detectors or sources. Furthermore, the high degree of spatial

confinement of SPhP optical modes could provide the basis for sub-diffraction, super-resolution imaging or reduced pixel size imagers. These properties also have high potential for enhanced molecular sensing and identification through the SEIRA process. Promising results by Anderson [125] support this claim. Further, an IR analog of surface plasmon resonance (SPR) biosensing was recently demonstrated by Neuner et al. [174] whereby changes in the local index of refraction on a SiC surface were detected by attenuated total reflection (ATR), and they enable detection of pL quantities of analytes (Figure 12A). In addition, the coincidence of the Reststrahlen band of hBN, c-BN, SiC, SiO₂, Al₂O₃ and many III-N materials with the vibrational modes of a wide array of molecular species and with an atmospheric transmission window leads to the potential for a wide array of applications. For instance, covert, stand-off molecular sensing and/or tagging, tracking and locating approaches could be realized. This atmospheric window also raises the potential for mid-IR free-space communications with improved detectors and sources. Based on the availability of SPhP materials exhibiting Reststrahlen bands over a broad spectral range overlapping with that of the most intense blackbody radiation, Rephaeli et al. [75] reported the potential for a broadband SPhP metamaterial shown in Figure 12B that would be capable of achieving cooling efficiencies in excess of 100 W/m² at room temperature.

Another area of importance is the role of thermal emitters and their potential as optical sources. As shown in Figure 5B and C, it was reported [51, 124, 176] that SPhP particles emit tailored thermal emission spectra that correspond to the localized SPhP resonances [23] and maintain the corresponding polarization of the optical modes in the far-field. Currently sources in the mid- and far-infrared are limited. For instance, in the mid-IR the primary emitters are either low-efficiency, broadband glowbars, such as those used in FTIR instruments, or more expensive coherent, monochromatic sources such as CO₂ or quantum cascade lasers, both of which offer some degree of wavelength tunability. Furthermore, narrow-band, polarized sources within the far-infrared are exceptional bulky, and require cryogenic cooling. Thus, there is significant desire for inexpensive, narrow-band and polarized sources that could be provided through nanostructured, polar dielectric materials via the corresponding modified black-body emission spectrum. Further, the incorporation of narrow apertures within SPhP materials around $\text{Re}(\epsilon)\sim 0$ could also potentially convert incident broadband infrared light into ultra-narrow bandwidth sources.

While outside of the scope of this review to discuss in detail, we note that many SPhP materials exhibit high birefringence and, in many cases, a natural hyperbolic

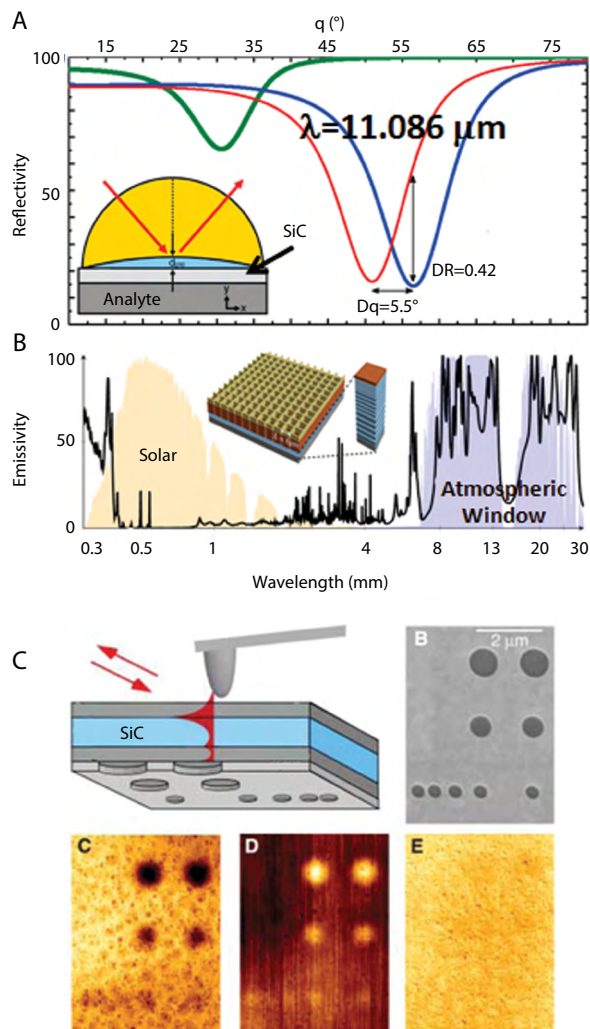


Figure 12 (A) Demonstration of infrared index-based biosensing using SPhP modes in SiC. (B) Schematic of the optimized daytime radiative cooler design based on SPhP materials SiC and SiO₂ along with MgF₂/TiO₂/Ag reflectors and the calculated emissivity of the structure at normal incidence (black curve). The AM1.5 solar spectrum and atmospheric transmittance window are also provided as the yellow and blue regions, respectively. (C) Schematic of SNOM-based detection scheme used to collect the superlens images of the sub-diffraction particles. Reproduced with permission from Ref. [174] (A), [75] (B), and [175] (C).

optical response. As discussed previously, hBN offers such behavior over two distinct spectral bands. The potential for hyperbolic media has been extensively discussed in the literature [80, 177, 178], however it has focused primarily on plasmonic/dielectric stacked systems, which typically exhibit high plasmonic losses and only support negative $\text{Re}(\epsilon)$ along one principal axis. In contrast, van der Waals crystals such as MoS₂, WS₂, etc [76], and other polar dielectrics [77] could potentially offer additional materials with

naturally reciprocal hyperbolic response [53]. Such optical behavior, coupled with the low-loss nature of the SPhP modes, could enable the realization of sub-diffraction and/or flat optics such as mid-IR polarizers, wave plates, etc. Furthermore, this provides the basis for hyperlenses [179] and superlenses [74, 175, 180] capable of super-resolution imaging within a single active layer, which in view of the low optical losses of these materials, may result in commercially attractive products for the mid-IR. Such a SPhP-based superlens was previously reported by Taubner et al. [175] and enabled the imaging of objects 20x smaller than the free-space wavelength as shown in Figure 12C.

As mentioned previously, propagating SPhP modes do not provide a direct benefit in terms of improved propagation lengths at a given confinement in comparison to metal-based SPP MIM or similar waveguide systems. However, the ability to support such modes within a simple, single material system can provide significant advantages. Further, multi-frequency waveguides using stacked layers of different, lattice-matched polar dielectric materials (e.g., GaN/AlN/SiC) may find attractive applications, such as multi-frequency localized resonators or as recently reported by Li et al. [74] as the basis for a multi-frequency superlens.

Finally, the relatively small values of $\text{Im}(\epsilon)$ [at a given $\text{Re}(\epsilon)$] by comparison with noble metals and doped semiconductors imply that SPhP should find applications as metamaterial constituents. The high Q's possible with many of the SPhP materials, and/or the exceptionally high index that is achievable for the frequencies just below ω_{TO} may also be employed to produce deeply sub-wavelength dielectric antennas and resonators [51], and novel metamaterial structures with multi-frequency and multi-functional operation. Furthermore, these properties could provide the basis for the realization of metatronic optical circuits initially proposed by Engheta [181] with nanostructures acting as wavelength-dependent optical inductors, capacitors and/or resistors for next generation circuits operating at optical frequencies.

Overall, polar dielectric materials and the SPhP modes they support provide not only a low-loss alternative to plasmonics, but open up many opportunities unachievable with plasmonic media, such as natural, reciprocal hyperbolic and birefringent response, modulation using doping and/or defects within the material, flexible operating wavelength ranges dependent upon the crystal properties as well as the dielectric and metal-like optical response from the same material. It is our hope that this review, along with the wealth of exceptional literature in the field of SPhP materials will lead to a reinvigoration of research in this area and to a realization of the promise that these materials offer.

Glossary

| | |
|--|---|
| SPP | surface plasmon polariton |
| SPhP | surface phonon polariton |
| SERS | surface enhanced Raman scattering |
| SEIRA | surface enhanced infrared absorption |
| TO | transverse optical phonon |
| LO | longitudinal optical phonon |
| LA | longitudinal acoustic phonon |
| FOM | figure of merit |
| THz | terahertz |
| IR | infrared |
| UV | ultraviolet |
| LSP | localized surface plasmon |
| Q | quality factor |
| IFC | interatomic force constants |
| λ_{res} | resonant wavelength |
| ω_p | plasma frequency |
| γ | oscillator damping constant |
| ϵ | complex permittivity |
| ϵ_m | complex permittivity of plasmonic material |
| ϵ_{SPhP} | complex permittivity of surface phonon polariton material |
| ϵ_a | complex permittivity of ambient or dielectric |
| $\text{Re}(\epsilon), \text{Im}(\epsilon)$ | real and imaginary permittivity |
| ϵ_0 | vacuum permittivity |
| ϵ_∞ | high-frequency permittivity |
| $\epsilon(0)$ | low-frequency permittivity |
| N | carrier density |
| e | electron charge |
| m^* | effective mass |
| r | radius |
| σ_{abs} | absorption cross-section |
| k | k-vector of photons |
| ω_{TO}, ω_{LO} | frequency of transverse and longitudinal optical phonons |
| s^2 | oscillator strength |
| n | index of refraction |
| ω_F | Frohlich frequency |
| $ E_{max} , E_{inc} $ | absolute value of the maximum and incident electric fields |
| $ U_{in} , U_{out} $ | electromagnetic energy inside and outside the SPP/SPhP material |
| L_p | polariton propagation length |
| L_m | vertical extent of polariton field |
| ω_o | frequency of maximum FOM value |
| ω_j | phonon frequency of phonon branch j |
| τ_j | phonon lifetime of phonon branch j |
| K | interatomic bond force constant |
| \vec{q} | phonon wavevector |
| N_0 | number of unit cells |
| Γ | phonon scattering rate |
| \vec{G} | reciprocal lattice vector |
| m_{light} and m_{heavy} | masses of light and heavy atoms in lattice |
| ω_A, ω_{Opt} | acoustic and optic vibrational frequencies at the Brillouin zone boundary |
| Z, Z^* | reduced and Born effective charges |

Acknowledgments: Support for all NRL authors was provided by the NRL Nanoscience Institute via Office of Naval

Research funding. J.D.C. would like to thank Prof. Alexander Grigorenko of the University of Manchester for his helpful advice in tailoring this manuscript to a broader audience. The authors would like to thank Prof. Alexandra Boltasseva, Mr. Jongbum Kim and Mr. Urcan Guler for sharing the optical constants of TiN, AZO, GZO and ITO for use in this review. We further thank Mr. Edward Sachet and Prof. Jon-Paul Maria of North Carolina State University for providing the optical constants of n-CdO for use in this review. We would also like to thank Dr. James Long, Joseph Tischler, Chase Ellis and Alex Boosalis for efforts in extracting optical constants of various SiC and III-N materials available at NRL. J.D.C. would like to thank Prof. Kostya Novoselov for access to his laboratory and office space at the University of Manchester where work on this review was undertaken and for access to hexagonal boron nitride materials for which the reported optical constants are derived. The authors also thank Dr. Kathryn Wahl and Jeffrey Owrutsky for access to the FTIR microscope used for the spectra provided in Figure 2A. L.L. acknowledges the financial support of the NRC-NRL Postdoctoral Fellowship. S.M. and V.G. acknowledge support from EPSRC and Leverhulme Trust.

References

- [1] Ritchie RH. Plasma losses by fast electrons in thin films. *Phys Rev Lett* 1957;106:874–81.
- [2] Fleischmann M, Hendra PJ, McQuillan AJ. Raman spectra of pyridine adsorbed at a silver electrode. *Chem Phys Lett* 1974;26:163–6.
- [3] Jeanmaire DL, van Duyne RP. Surface raman electrochemistry part I: heterocyclic, aromatic and aliphatic amines adsorbed on the anodized silver electrode. *J Electroanal Chem* 1977;84:1–20.
- [4] Ebbesen TW, Lezec HJ, Ghaemi HF, Thio T, Wolff PA. Extraordinary optical transmission through sub-wavelength hole arrays. *Nature* 1998;391:667–9.
- [5] Brongersma ML, Kik PG. *Surface plasmon nanophotonics*. New York: Springer, 2010.
- [6] Engheta N, Ziolkowski RW. *Metamaterials: physics and engineering explorations*. Hoboken, NJ: Wiley & Sons, 2006.
- [7] Caldwell JD, Glembocki OJ, Bezares FJ, Bassim ND, Rendell RW, Feygelson M, Ukaegbu M, Kasica R, Shirey L, Hosten C. Plasmonic nanopillar arrays for large-area, high enhancement surface-enhanced raman scattering sensors. *ACS Nano* 2011;5:4046–55.
- [8] Caldwell JD, Glembocki OJ, Bezares FJ, Kariniemi MI, Niinistö JT, Hatanpää TT. Large-area plasmonic hot-spot arrays: Sub-2 nm interpillar spacings with plasma enhanced atomic layer deposition of Ag on periodic arrays of Si nanopillars. *Opt Express* 2011;19:26056.
- [9] Kneipp K, Wang Y, Kneipp H, Perelman LT, Itzkan I, Dasari RR, Feld MS. Single molecule detection using surface-enhanced Raman scattering. *Phys Rev Lett* 1997;78:1667.

- [10] Nie S, Emory SR. Probing single molecules and single nanoparticles by surface-enhanced Raman scattering. *Science* 1997;275:1101.
- [11] Atwater HA, Polman A. Plasmonics for improved photovoltaic devices. *Nat Mater* 2010;9:205–13.
- [12] Aubry A, Lei DY, Fernandez-Dominguez AI, Sonnefraud Y, Maier SA, Pendry JB. Plasmonic light-harvesting devices over the whole visible spectrum. *Nano Lett* 2010;10:2574–9.
- [13] Mooney JM, Silverman J. The theory of hot-electron photoemission in Schottky-barrier IR detectors. *IEEE T Electron Dev* 1985;32:33–9.
- [14] Clavero C. Plasmon-induced hot-electron generation at nanoparticle/metal-oxide interfaces for photovoltaic and photocatalytic devices. *Nature Photon* 2014;8:95–103.
- [15] Sobhani A, Knight MW, Wang Y, Brown LV, Fang Z, Nordlander P, Halas NJ. Narrowband photodetection in the near-infrared with a plasmon-induced hot electron device. *Nat Commun* 2013;4:1643.
- [16] Goykhman I, Desiatov B, Khurgin JB, Shappir J, Levy U. Locally Oxidized Silicon Surface-Plasmon Schottky Detector for Telecom Regime. *Nano Lett* 2011;11:2219–24.
- [17] Khurgin JB, Boltasseva A. Reflecting upon the losses in plasmonics and metamaterials. *MRS Bull* 2012;37:768–79.
- [18] Khurgin JB, Sun G. In search of the elusive lossless metal. *Appl Phys Lett* 2010;96:181102.
- [19] Khurgin JB, Sun G. Scaling of losses with size and wavelength in nanoplasmonics and metamaterials. *Appl Phys Lett* 2011;99:211106.
- [20] Hillenbrand R, Taubner T, Keilmann F. Phonon-enhanced light-matter interaction at the nanometre scale. *Nature* 2002;418:159–62.
- [21] Boltasseva A, Atwater HA. Low-loss plasmonic metamaterials. *Science (Wash.)* 2011;331:290–1.
- [22] West PR, Ishii S, Naik GV, Emani NK, Shalae VM, Boltasseva A. Searching for better plasmonic materials. *Laser Photon Rev* 2010;4:795–808.
- [23] Caldwell JD, Glembocki OJ, Sharac N, Giannini V, Bezares FJ, Long JP, Owrutsky JC, Vurgaftman I, Tischler JG, Wheeler VD, Bassim ND, Shirey LM, Kasica R, Maier SA. Low-loss, extreme sub-diffraction photon confinement via silicon carbide surface phonon polariton nanopillar resonators. *Nano Lett* 2013;13:3690–7.
- [24] Feurer T, Stoyanov NS, Ward DW, Vaughan JC, Stutz ER, Nelson KA. Terahertz polaritonics. *Ann Rev Mater Res* 2007;37:317–50.
- [25] Hillenbrand R. Towards Phonon Photonics: Scattering-type near-field optical microscopy reveals phonon-enhanced near-field interaction. *Ultramicroscopy* 2004;100:421–7.
- [26] Guler U, Ndukaiife JC, Naik GV, Agwu Nnanna AG, Kildishev AV, Shalae VM, Boltasseva A. Local heating with lithographically fabricated plasmonic titanium nitride nanoparticles. *Nano Lett* 2013;13:6078–83.
- [27] Naik GV, Schroeder JL, Ni X, Kildishev AV, Sands TD, Boltassev A. Titanium nitride as a plasmonic material for visible and near-infrared wavelengths. *Opt Mater Express* 2012;2:478–89.
- [28] Blaber MG, Arnold MD, Ford MJ. A review of the optical properties of alloys and intermetallics for plasmonics. *J Phys: Condens Matter* 2010;22:143201.
- [29] Escarra MD, Thongrattanasiri S, Charles WO, Hoffman AJ, Podolskiy VA, Gmachl C. Enhanced bandwidth and reduced dispersion through stacking multiple optical metamaterials. *Opt Express* 2011;19:14990–8.
- [30] Kim H, Osofsky M, Prokes SM, Glembocki OJ, Pique A. Optimization of Al-doped ZnO films for low-loss plasmonic materials at telecommunications wavelengths. *Appl Phys Lett* 2013;102:171103.
- [31] Kim J, Naik GV, Emani NK, Guler U, Boltasseva A. Plasmonic resonances in nanostructured transparent conducting oxide films. *IEEE J Sel Top Quant Electron* 2013;19:4601907.
- [32] Kim J, Naik GV, Shalae VM, Gavrilenko AV, Dondapati K, Gavrilenko VI, Prokes SM, Glembocki OJ, Boltasseva A. Optical properties of gallium-doped zinc oxide—a low-loss plasmonic material: first principles theory and experiment. *Phys Rev X* 2014;3:041037.
- [33] Sachet E, Maria J-P. Mid-IR Plasmonics with n-type CdO. 2014, Private communication.
- [34] Maier SA. Graphene plasmonics all eyes on flatland. *Nat Phys* 2012;8:581–2.
- [35] Grigorenko AN, Polini M, Novoselov KS. Graphene plasmonics. *Nature Photon* 2012;6:749–58.
- [36] Chen J, Badioli M, Alonso-Gonzalez P, Thongrattanasiri S, Huth F, Osmond J, Spasenovic M, Centeno A, Pesquera A, Godignon P, Elorza AZ, Camara N, Garcia de Abajo JF, Hillenbrand R, Koppens FHL. Optical nano-imaging of gate-tunable graphene plasmons. *Nature* 2012;487:77–81.
- [37] Koppens FHL, Chang DE, Garcia de Abajo FJ. Graphene plasmonics: a platform for strong light-matter interactions. *Nano Lett* 2011;11:3370–7.
- [38] Fei Z, Rodin AS, Andreev GO, Bao W, McLeod AS, Wagner M, Zhang LM, Zhao Z, Thiemens M, Dominguez G, Fogler MM, Castro Neto AH, Lau CN, Keilmann F, Basov DN. Gate-tuning of graphene plasmons revealed by infrared nano-imaging. *Nature* 2012;487:82–5.
- [39] Vakil A, Engheta N. Transformation optics using graphene. *Science (Wash.)* 2011;332:1291–4.
- [40] Basov DN, Fogler MM, Lanzara A, Wang F, Zhang Y. Colloquium: graphene spectroscopy. *RvMP* 2014;86:959–94.
- [41] Scharfe M, Porath R, Ohms T, Aeschlimann M, Krenn JR, Dittlbacher H, Aussenegg FR, Liebsch A. Do Mie plasmons have a longer lifetime on resonance than off resonance? *Appl Phys B* 2001;73:305–10.
- [42] Kreibitz U, Vollmer M. *Optical properties of metal clusters*. Berlin: Springer, 2010.
- [43] Bosman M, Ye E, Tan SF, Nijhuis CA, Yang JKW, Marty R, Mlayah A, Arbouet A, Girard C, Han M-Y. Surface plasmon damping quantified with an electron nanoprobe. *Sci Rep* 2013;3:1312.
- [44] Wells SM, Merkulov IA, Kravchenko II, Lavrik NV, Sepaniak MJ. Silicon nanopillars for field-enhanced surface spectroscopy. *ACS Nano* 2012;6:2948–59.
- [45] Bezares FJ, Long JP, Glembocki OJ, Guo J, Rendell RW, Kasica R, Shirey L, Owrutsky JC, Caldwell JD. Mie resonance-enhanced light absorption in periodic silicon nanopillar arrays. *Opt Express* 2013;21:27587–601.
- [46] Spinelli P, Verschuuren MA, Polman A. Broadband omnidirectional antireflection coating based on subwavelength surface Mie resonators. *Nat Commun* 2012;3:692.
- [47] Zhao Q, Zhou J, Zhang F, Lippens D. Mie Resonance-based dielectric metamaterials. *mater. Today* 2009;12:60–9.
- [48] Moitra P, Yang Y, Anderson Z, Kravchenko II, Briggs D, Valentine, J. Realization of an All-dielectric Zero-index Optical Metamaterial. *Nature Photonics* 2013;7:791–5.

- [49] Valentine J, Li J, Zentgraf T, Bartal G, Zhang X. An optical cloak made of dielectrics. *Nature Materials* 2009;8:568–71.
- [50] Ginn JC, Brener I, Peters DW, Wendt JR, Stevens JO, Hines PF, Basilio LI, Warne LK, Ihlefeld JF, Clem PG, Sinclair MB. Realizing optical magnetism from dielectric metamaterials. *Phys Rev Lett* 2012;108:097402.
- [51] Schuller JA, Taubner T, Brongersma ML. Optical antenna thermal emitters. *Nature Photon* 2009;3:658–61.
- [52] Geick R, Perry CH, Rupprecht G. Normal modes in hexagonal boron nitride. *Phys Rev B* 1966;146:543–7.
- [53] Caldwell JD, Kretinin A, Chen Y, Giannini V, Fogler MM, Francescato Y, Ellis CT, Tischler JG, Woods CR, Giles AJ, Hong M, Watanabe K, Taniguchi T, Maier SA, Novoselov KS. Sub-diffractive, volume-confined polaritons in the natural hyperbolic material hexagonal boron nitride. 2014;arXiv:1404.0494 (in press).
- [54] Dai S, Fei Z, Ma Q, Rodin AS, Wagner M, McLeod AS, Liu MK, Gannett W, Regan W, Watanabe K, Taniguchi T, Thiemens M, Dominguez G, Castro Neto AH, Zettl A, Keilmann F, Jarillo-Herrero P, Fogler MM, Basov DN. Tunable phonon polaritons in atomically thin van der Waals crystals of boron nitride. *Science (Wash.)* 2014;343:1125–9.
- [55] Cai Y, Zhang LM, Zeng Q, Cheng L, Xu Y. Infrared reflectance spectrum of BN calculated from first principles. *Solid State Commun* 2007;141:262–6.
- [56] Pitman KM, Speck AK, Hofmeister AM, Corman AB. Optical properties and applications of silicon carbide in astrophysics. In: Mukherjee M, ed. *Silicon carbide-materials, processing and applications in electronic devices*. ed. Rijeka, Croatia: InTech, 2011.
- [57] Tiwald TE, Woolam JA, Zollner S, Christiansen J, Gregory RB, Wetteroth T, Wilson SR, Powell AR. Carrier concentration and lattice absorption in bulk and epitaxial silicon carbide determined using infrared ellipsometry. *Phys Rev B* 1999;60:11464–74.
- [58] Haraguchi M, Fukui M, Muto S. Experimental observation of attenuated-total-reflection spectra of a GaAs/AlAs superlattice. *Phys Rev B* 1990;41:1254–7.
- [59] Moore WJ, Holm RT. Infrared dielectric constant of GaAs. *J Appl Phys* 1996;80:6939–42.
- [60] Yu PY, Cardona M. *Fundamentals of semiconductors: physics and materials properties*. New York, NY: Springer, 1999.
- [61] Passerat de Silans T, Maurin I, Chaves de Souza Segundo P, Saltiel S, Gorza M-P, Ducloy M, Bloch D, Meneses D, Echegut P. Temperature dependence of the dielectric permittivity of CaF_2 , BaF_2 and Al_2O_3 : application to the prediction of a temperature-dependence van der Waals surface interaction exerted onto a neighbouring $\text{Cs}(8\text{P}_{3/2})$ atom. *J Phys: Condens Matter* 2009;21:255902.
- [62] Adachi S. *The reststrahlen region. Optical properties of crystalline and amorphous semiconductors: materials and fundamental principles*. ed. New York, NY: Springer Science+Business Media, LLC, 1999, 33–61.
- [63] Bohren CF, Huffman DR. *Absorption and scattering of light by small particles*. Weinheim, Germany, John Wiley & Sons, Inc., 2004, 331–44.
- [64] Wang T, Li P, Hauer B, Chigrin DN, Taubner T. Optical properties of single infrared resonant circular microcavities for surface phonon polaritons. *Nano Lett* 2013;13:5051–5.
- [65] Nagpal P, Lindquist NC, Oh S-H, Norris DJ. Ultrasubwavelength patterned metals for plasmonics and metamaterials. *Science (Wash.)* 2009;325:594–7.
- [66] Lu Y-J, Kim J-Y, Chen H-Y, Wu C, Dabidian N, Sanders CE, Wang C-Y, Lu M-Y, Li B-H, Qiu X, Chang W-H, Chen L-J, Shvets G, Shih C-H, Gwo S. Plasmonic nanolaser using epitaxially grown silver film. *Science (Wash.)* 2012;337:450–3.
- [67] Kariniemi M, Niinistö J, Hatanpää T, Kemell M, Sajavaara T, Ritala M, Leskelä M. Plasma-enhanced atomic layer deposition of silver thin films. *Chem Mater* 2011;23:2901–7.
- [68] Prokes SM, Glembocki OJ, Cleveland E, Caldwell JD, Foss E, Niinistö J, Ritala M. Spoof-like plasmonic behavior of plasma enhanced atomic layer deposition grown Ag thin films. *Appl Phys Lett* 2012;100:053106.
- [69] Caldwell JD, Stahlbush RE, Mahadik NA. Mitigating defects within silicon carbide epitaxy. *J Electrochem Soc* 2012;159:R46–51.
- [70] Skowronski M, Ha S. Degradation of hexagonal silicon-carbide-based bipolar devices. *J Appl Phys* 2006;99:011101.
- [71] Stevenson R. The world's best gallium nitride. *IEEEES* 2010;47:40–5.
- [72] Eddy CR, Nepal N, Hite JK, Mastro MA. Perspectives on future directions in III-N semiconductor research. *J Vac Sci Technol A* 2013;31:058501.
- [73] Silveirinha MG, Engheta N. Tunneling of electromagnetic energy through sub-wavelength channels and bends using epsilon-near-zero (ENZ) materials. *Phys Rev Lett* 2006;97:157403.
- [74] Li P, Taubner T. Multi-wavelength superlensing with layered phonon-resonant dielectrics. *Opt Express* 2012;20:A11787.
- [75] Rephaeli E, Raman A, Fan S. Ultrabroadband photonic structures to achieve high-performance daytime radiative cooling. *Nano Lett* 2013;13:1457–61.
- [76] Geim AK, Grigorieva IV. Van der Waals heterostructures. *Nature* 2013;499:419–25.
- [77] Sun J, Litchinitser NM, Zhou J. Indefinite by nature: from ultraviolet to terahertz. *ACS Photon* 2014;1:293–303.
- [78] Drachev VP, Podolskiy VA, Kildishev AV. Hyperbolic metamaterials: new physics behind a classical problem. *Opt Express* 2013;21:15048–64.
- [79] Guo Y, Newman W, Cortes CL, Jacob Z. Applications of hyperbolic metamaterial substrates. *Adv Opto Electron* 2012;2012:452502.
- [80] Jacob Z, Kim J-Y, Naik GV, Boltasseva A, Narimanov EE, Shalaev VM. Engineering photonic density of states using metamaterials. *ApPPL* 2010;100:215–8.
- [81] Korobkin D, Neuner B, Fietz C, Jegenyés N, Ferro G, Shvets G. Measurements of the negative refractive index of sub-diffraction waves propagating in an indefinite permittivity medium. *Opt Express* 2010;18:22734–46.
- [82] Enoch S, Bonud N. *Plasmonics: from basics to advanced topics*. Springer Series in Optical Sciences 2012;167.
- [83] Giannini V, Fernandez-Dominguez AI, Heck SC, Maier SA. Plasmonic nanoantennas: fundamentals and their use in controlling the radiative properties of nanoemitters. *Chem Rev* 2011;111:3888–912.
- [84] Gramotnev DK, Bozhevolnyi SI. Plasmonics beyond the diffraction limit. *Nature Photon* 2010;4:83–91.
- [85] Hayashi S, Okamoto T. Plasmonics: visit the past to know the future. *JPhD* 2012;45:433001.
- [86] Maier SA. *Plasmonics: fundamentals and applications*. Berlin: Springer, 2007.
- [87] Rendell RW, Scalapino DJ, Mulschlegel B. Role of local plasmon modes in light emission from small particle tunnel junctions. *Phys Rev Lett* 1978;41:1746.

- [88] Rendell RW, Scalapino DJ. Surface plasmons confined by microstructures on tunnel junctions. *Phys Rev B* 1981;24:3276.
- [89] Palik ED. Handbook of optical constants of solids. Orlando: Elsevier, 1985.
- [90] Johnson PB, Christy RW. Optical constants of the noble metals. *Phys Rev B* 1972;6:4370.
- [91] Chen Y, Francescato Y, Caldwell JD, Giannini V, Maß TWW, Glembocki OJ, Bezares FJ, Taubner T, Kasica R, Hong M, Maier SA. Spectral tuning of localized surface phonon polariton resonators for low-loss mid-IR applications. *ACS Photon* 2014;1:718–24.
- [92] Huber AJ, Deutsch B, Novotny L, Hillenbrand R. Focusing of surface phonon polaritons. *Appl Phys Lett* 2008;92:203104.
- [93] Ng SS, Hassan Z, Abu Hassan H. Surface phonon polariton of wurtzite GaN thin film grown on c-plane sapphire substrate. *Solid State Commun* 2008;145:535–8.
- [94] Lahiri B, Holland G, Aksyuk V, Centrone A. Nanoscale imaging of plasmonic hot spots and dark modes with the photothermal-induced resonance technique. *Nano Lett* 2013;13:3218–24.
- [95] Schuller JA, Zia R, Taubner T, Brongersma ML. Dielectric metamaterials based on electric and magnetic resonances of silicon carbide particles. *Phys Rev Lett* 2007;99:107401.
- [96] Ruppin R, Englman R. Optical phonons of small crystals. *Rep Prog Phys* 1970;33:149–96.
- [97] Wang F, Shen YR. General properties of local plasmons in metal nanostructures. *Phys Rev Lett* 2006;97:206806.
- [98] Khurgin JB, Sun G. Enhancement of optical properties of nanostructured objects by metal nanoparticles. *J Opt Soc Am B* 2009;26:B83–95.
- [99] Simpkins BS, Long JP, Glembocki OJ, Guo J, Caldwell JD, Owrutsky JC. Pitch-dependent resonances and coupling regimes in nanoantenna arrays. *Opt Express* 2012;20:27725–39.
- [100] Stockman MI, Pandey LN, George TF. Inhomogeneous localization of polar eigenmodes in fractals. *Phys Rev B: Condens Matter* 1996;53:2183.
- [101] Kottman JP, Martin OJF. Plasmon resonant coupling in metallic nanowires. *Opt Express* 2001;8:655.
- [102] Khanikaev AB, Wu C, Shvets G. Fano-resonant metamaterials and their applications. *Nanophotonics* 2013;2:247–64.
- [103] Luk'yanchuk B, Zheludev NI, Maier SA, Halas NJ, Nordlander P, Giessen H, Chong CT. The fano resonance in plasmonic nanostructures and metamaterials. *Nat Mater* 2010;9:707–15.
- [104] Adato R, Yanik AA, Amsden JJ, Kaplan DL, Omenetto FG, Hong MK, Erramilli S, Altug H. Ultra-sensitive vibrational spectroscopy of protein monolayers with plasmonic nanoantenna arrays. *Proc Natl Acad Sci USA* 2009;106:19227–32.
- [105] Kullock R, Grafstrom S, Evans PR, Pollard RJ, Eng LM. Metallic nanorod arrays: negative refraction and optical properties explained by retarded dipolar interactions. *J Opt Soc Am B: Opt Phys* 2001;27:1819–27.
- [106] Kravets VG, Schedin F, Grigorenko AN. Extremely narrow plasmon resonances based on diffraction coupling of localized plasmons in arrays of metallic nanoparticles. *Phys Rev Lett* 2008;101:087403.
- [107] Kravets VG, Schedin F, Kabashin AV, Grigorenko AN. Sensitivity of collective plasmon modes of gold nanoresonators to local environment. *Opt Lett* 2010;35:956–8.
- [108] Ciraci C, Hill RT, Mock JJ, Urzhumov Y, Fernández-Domínguez AI, Maier SA, Pendry JB, Chilkoti A, Smith DR. Probing the ultimate limits of plasmonic enhancement. *Science (Wash.)* 2012;337:1072–4.
- [109] Ordal MA, Long LL, Bell RJ, Bell SE, Bell RR, Alexander, Jr. RW, Ward CA. Optical properties of the metals Al, Co, Cu, Au, Fe, Pb, Ni, Pd, Pt, Ag, Ti, and W in the infrared and far infrared. *Appl Opt* 1983;22:1099–120.
- [110] Rakic AD. Algorithm for the determination of intrinsic optical constants of metal films: application to aluminum. *Appl Opt* 1995;34:4755–67.
- [111] Schubert M, Rheinlander B, Franke E, Neumann H, Tiwald TE, Woolam JA, Hahn J, Richter F. Infrared optical properties of mixed-phase thin films studied by spectroscopic ellipsometry using boron nitride as an example. *Phys Rev B* 1997;56:13306–13.
- [112] Moore WJ, Holm RT, Yang MJ, Freitas JA. Infrared dielectric constant of cubic SiC. *J Appl Phys* 1995;78:7255–8.
- [113] Kazan M, Pereira S, Correia MR, Masri P. Directional dependence of AlN intrinsic complex dielectric function, optical phonon lifetimes and decay channels measured by polarized infrared reflectivity. *J Appl Phys* 2009;106:023523.
- [114] Schubert M, Tiwald TE, Herzinger CM. Infrared dielectric anisotropy and phonon modes of sapphire. *Phys Rev B* 2000;61:8187–201.
- [115] Kasic A, Schubert M, Einfeldt S, Hommel D, Tiwald TE. Free-carrier and phonon properties of n- and p-type hexagonal GaN films measured by infrared ellipsometry. *Phys Rev B* 2000;62:7365–77.
- [116] Ashkenov N, Mbenkum BN, Bundesmann C, Riede V, Lorenz M, Spemann D, Kaidashev EM, Kasic A, Schubert M, Grundmann M, Wagner G, Neumann H, Darakchieva V, Arwin H, Monemar B. Infrared dielectric functions and phonon modes of high-quality ZnO films. *J Appl Phys* 2003;93:126–33.
- [117] Jahne E, Roseler A, Ploog K. Infrared reflectance and ellipsometric studies of GaAs/AlAs superlattices. *Superlattices Microstruct* 1991;9:219–22.
- [118] Adams DC, Inampudi S, Ribaudo T, Slocum D, Vangala S, Kuhta NA, Goodhue WD, Podolskiy VA, Wasserman D. Funneling light through a subwavelength aperture with epsilon near zero materials. *Phys Rev Lett* 2011;107:133901.
- [119] Hoffman AJ, Alekseyev L, Howard SS, Franz KJ, Wasserman D, Podolskiy VA, Narimanov EE, Sivco DL, Gmach C. Negative refraction in semiconductor metamaterials. *Nat Mater* 2007;6:946–50.
- [120] Naik GV, Shalaev VM, Boltasseva A. Alternative plasmonic materials: beyond gold and silver. *Adv Mater* 2013;25:3264–94.
- [121] Harima H, Nakashima S-I, Uemura T. Raman scattering from anisotropic LO-phonon-plasmon-coupled mode in n-type 4H- and 6H-SiC. *J Appl Phys* 1995;78:1996.
- [122] Caldwell JD, Glembocki OJ, Prokes SM, Glaser ER, Hobart KD, Hansen DM, Chung GY, Bolotnikov AV, Sudarshan TS. Free carrier distribution profiling of 4H-SiC substrates using a commercial optical scanner. *J Appl Phys* 2007;101:093506.
- [123] Mutschke H, Anderson AC, Clement D, Henning T, Peiter G. Infrared properties of SiC particles. *Astron Astrophys* 1999;345:187–202.
- [124] Greffet J-J, Carminati R, Joulain K, Mulet JP, Mainguy S, Chen Y. Coherent emission of light by thermal sources. *Nature* 2002;416:61–4.
- [125] Anderson MS. Enhanced infrared absorption with dielectric nanoparticles. *Appl Phys Lett* 2003;83:2964–6.

- [126] Berini P. Figures of merit for surface plasmon waveguides. *Opt Express* 2006;14:13030–42.
- [127] Oulton RF, Sorger VJ, Genov DA, Pile DFP, Zhang X. A hybrid plasmonic waveguide for subwavelength confinement and long-range propagation. *Nature Photon* 2008;2:496.
- [128] Bennett HE, Bennett JM. Optical properties and electronic structure of metals and alloys. Amsterdam: North-Holland, 1966.
- [129] Holmstrom SA, Stievater TH, Pruessner MW, Park D, Rabinovich WR, Khurgin JB, Richardson CJK, Kanakaraju S, Calhoun LC, Ghodssi R. Guided-mode phonon-polaritons in suspended waveguides. *Phys Rev B* 2012;86:165120.
- [130] Urzhumov Y, Korobkin D, Neuner B, Zorman C, Shvets G. Optical properties of sub-wavelength hole arrays in SiC membranes. *JOptA* 2007;9:S322–3.
- [131] Li D, Lawandy NM, Zia R. Surface phonon-polariton enhanced optical forces in silicon carbide nanostructures. *Opt Express* 2013;21:20900–10.
- [132] Nilsson G, Nelin G. Study of homology between silicon and germanium by thermal-neutron spectrometry. *Phys Rev B* 1972;6:3777–86.
- [133] Feldman DW, Parker JH, Choyke WJ, Patrick L. Phonon dispersion curves by Raman scattering in SiC polytypes 3C, 4H, 6H, 15R, and 21R. *Phys Rev B* 1968;173:787–93.
- [134] Baroni S, Gironcoli S, A. Dal Corso and Giannozzi P. Phonons and related crystal properties from density-functional perturbation theory. *RvMP* 2001;73:515–62.
- [135] Ziman JM. Electrons and phonons. London: Oxford University Press, 1960.
- [136] Ashcroft NW, Mermin ND. Solid state physics. USA: Brooks/Cole, 1976.
- [137] Kittel C. Introduction to solid state physics. Hoboken: John Wiley and Sons, Inc., 1996.
- [138] Warren JL, Yarnell JL, Dolling G, Cowley RA. Lattice dynamics of diamond. *Phys Rev B* 1967;158:805–8.
- [139] Sanjurjo JA, E. Lopez-Cruz, Vogl P, Cardona M. Dependence on volume of the phonon frequencies and their effective charges of several III-V semiconductors. *Phys Rev B* 1983;28:4579–84.
- [140] Reich S, Ferrari AC, Arenal R, Loiseau A, Bello I, Robertson J. Resonant raman scattering in cubic and hexagonal boron nitride. *Phys Rev B* 2005;71:205201.
- [141] Deinzer G, Schmitt M, Mayer AP, Strauch D. Intrinsic lifetimes and anharmonic frequency shifts of long-wavelength optical phonons in polar crystals. *Phys Rev B* 2004;69:014304.
- [142] Broido DA, Malorny M, Birner G, Mingo N, Steward DA. Intrinsic lattice thermal conductivity of semiconductors from first principles. *Appl Phys Lett* 2007;91:231922.
- [143] Ecsedy DJ, Klemens PG. Thermal resistivity of dielectric crystals due to 4-phonon processes and optical modes. *Phys Rev B* 1977;15:5957–62.
- [144] Lindsay L, Broido DA. Three-phonon phase space and lattice thermal conductivity in semiconductors. *J Phys: Condens Matter* 2008;20:165209.
- [145] Menendez J, Cardona M. Temperature-dependence of the 1st-Order Raman-Scattering by Phonons in Si, Ge, and A-Sn Anharmonic Effects. *Phys Rev B* 1984;29:2051–9.
- [146] Kuhl J, Bron WE. Temperature-dependence of longitudinal optical phonon lifetimes in GaP. *Solid State Commun* 1984;49:935–8.
- [147] Vallee F, Bogani F. Coherent time-resolved investigation of LO-phonon dynamics in GaAs. *Phys Rev B* 1991;43:12049–52.
- [148] Vallee F. Time-resolved investigation of coherent LO-phonon relaxation in III-V semiconductors. *Phys Rev B* 1994;49:2460–8.
- [149] Anand S, Verma P, Jain KP, Abbi SC. Temperature dependence of optical phonon lifetimes in ZnSe. *PhyB* 1996;226:331–7.
- [150] Irmer G, Wenzel M, Monecke J. The temperature dependence of the LO (Γ) and TO (Γ) phonons in GaAs and InP. *PSSBR* 1996;195:85–95.
- [151] Bergman L, Alexson D, Murphy PL, Nemanich RJ, Dutta M, Stroschio MA, Balkas C, Shin H, Davis RF. Raman analysis of phonon lifetimes in AlN and GaN of wurtzite structure. *Phys Rev B* 1999;59:12977–82.
- [152] Kuball M, Hayes JM, Shi Y, Edgar JH. Phonon lifetimes in bulk AlN and their temperature dependence. *Appl Phys Lett* 2000;77:1958–60.
- [153] Pomeroy JW, Kuball M, Lu H, Schaff WJ, Wang X, Yoshikawa A. Phonon lifetimes and phonon decay in InN. *Appl Phys Lett* 2005;86:223501.
- [154] Song DY, Holtz M, Chandolu A, Nikishin SA, Mokhov EN, Makarov Y, Helava H. Optical phonon decay in bulk aluminum nitride. *Appl Phys Lett* 2006;89:021901.
- [155] Dyson A, Ridley BK. Phonon-plasmon coupled-mode lifetime in semiconductors. *J Appl Phys* 2008;103:114507.
- [156] Debernardi A, Baroni S, Molinari E. Anharmonic phonon lifetimes in semiconductors from density-functional perturbation-theory. *Phys Rev Lett* 1995;75:1819–22.
- [157] Debernardi A. Phonon linewidth in III-V semiconductors from density-functional perturbation theory. *Phys Rev B* 1998;57:12847–58.
- [158] Bonini N, Lazzeri M, Marzari N, Mauri F. Phonon anharmonicities in graphite and graphene. *Phys Rev Lett* 2007;99:176802.
- [159] Lindsay L, Broido DA, Reinecke TL. Ab-initio thermal transport in compound semiconductors. *Phys Rev B* 2013;87:165201.
- [160] Lindsay L, Broido DA, Reinecke TL. Phonon-isotope scattering and thermal conductivity in materials with a large isotope effect: A first-principles study. *Phys Rev B* 2013;88:144306.
- [161] Huber AJ, Ocelic N, Taubner T, Hillenbrand R. Nanoscale resolved infrared probing of crystal structure and of plasmon-phonon coupling. *Nano Lett* 2006;6:774–8.
- [162] Ocelic N, Hillenbrand R. Subwavelength-scale tailoring of surface phonon polaritons by focused ion-beam implantation. *Nat Mater* 2004;3:606–9.
- [163] Sridhara SG, Carlsson FHC, Bergman JP, Janzen E. Luminescence from stacking faults in 4H-SiC. *Appl Phys Lett* 2001;79:3944.
- [164] Stahlbush RE, Fatemi M, Fedison JB, Arthur SD, Rowland LB, Wang S. Stacking-fault formation and propagation in 4H-SiC PiN diodes. *J Electron Mater* 2002;31:370.
- [165] Caldwell JD, Klein PB, Twigg ME, Stahlbush RE. Observation of a multilayer planar in-grown stacking fault in 4H-SiC p-i-n diodes. *Appl Phys Lett* 2006;89:103519.
- [166] Caldwell JD, Liu KX, Tadjer MJ, Glembocki OJ, Stahlbush RE, Hobart KD, Kub F. Thermal annealing and propagation of shockley stacking faults in 4H-SiC PiN diodes. *J Electron Mater* 2007;36:318.
- [167] Caldwell JD, Stahlbush RE, Glembocki OJ, Ancona MG, Hobart KD. On the driving force for recombination-induced stacking fault motion in 4H-SiC. *J Appl Phys* 2010;108:044503.
- [168] Caldwell JD, Stahlbush RE, Hobart KD, Glembocki OJ, Liu KX. Reversal of forward voltage drift in 4H-SiC p-i-n diodes via low temperature annealing. *Appl Phys Lett* 2007;90:143519.

- [169] Galeckas A, Linnros J, Pirouz P. Recombination-induced stacking faults: evidence for a general mechanism in hexagonal SiC. *Phys Rev Lett* 2006;96:025502.
- [170] Ha S, Skowronski M, Sumakeris JJ, Paisley MJ, Das MK. Driving force of stacking-fault formation in SiC P-i-N diodes. *Phys Rev Lett* 2004;92:175504.
- [171] Iwata HP, Lindefelt U, Oberg S, Briddon PR. Stacking faults in silicon carbide. *Physica B* 2003;340:165–70.
- [172] Maximenko SI, Freitas JA, Klein PB, Shrivastava A, Sudarshan TS. Cathodoluminescence study of the properties of stacking faults in 4H-SiC homoepitaxial layers. *Appl Phys Lett* 2009;94:092101.
- [173] Bergman JP, Lendenmann H, Nilsson PA, Lindefelt U, Skytt P. Crystal defects as source of anomalous forward voltage increase of 4H-SiC diodes. *Mater Sci Forum* 2001;353–356:299–302.
- [174] Neuner B, Korobkin D, Fietz C, Carole D, Ferro G, Shvets G. Midinfrared index sensing of pL-scale analytes based on surface phonon polaritons in silicon carbide. *J Phys Chem C* 2010;114:7489–91.
- [175] Taubner T, Korobkin D, Urzhumov Y, Shvets G, Hillenbrand R. Near-field microscopy through a SiC superlens. *Science (Wash.)* 2006;313:1595.
- [176] Neuner B, Wu C, Eyck GT, Sinclair M, Brener I, Shvets G. Efficient infrared thermal emitters based on low-albedo polaritonic meta-surfaces. *Appl Phys Lett* 2013;102:211111.
- [177] Poddubny A, Iorsh I, Belov P, Kivshar Y. Hyperbolic metamaterials. *Nature Photon* 2013;7:958–67.
- [178] Yang X, Yao J, Rho J, Xiaobo Y, Zhang X. Experimental realization of three-dimensional indefinite cavities at the nanoscale with anomalous scaling laws. *Nature Photon* 2012;6:450–3.
- [179] Liu Z, Lee H, Xiong Y, Sun C, Zhang X. Far-field optical hyperlens magnifying sub-diffraction limited objects. *Science* 2007;315:1686.
- [180] Smith DR. How to build a superlens. *Science* 2005;308:502–3.
- [181] Engheta N. Circuits with light at nanoscales: optical nanocircuits inspired by metamaterials. *Science (Wash.)* 2007;317:1698–702.